CrossMark

J. Fluid Mech. (2019), *vol.* 864, *pp.* 519–553. © Cambridge University Press 2019
doi:10.1017/jfm.2018.999

Penetration of boundary-driven flows into a rotating spherical thermally stratified fluid

Grace A. Cox[1,2,3,†], Christopher J. Davies[4], Philip W. Livermore[4] and James Singleton[4]

[1]School of Environmental Sciences, University of Liverpool, Liverpool L69 3GP, UK

[2]Department of Applied Mathematics, University of Leeds, Leeds LS2 9JT, UK

[3]Dublin Institute for Advanced Studies, Geophysics Section, Dublin 2, Ireland

[4]School of Earth and Environment, University of Leeds, Leeds LS2 9JT, UK

(Received 23 February 2018; revised 23 October 2018; accepted 5 December 2018; first published online 11 February 2019)

Motivated by the dynamics within terrestrial bodies, we consider a rotating, strongly thermally stratified fluid within a spherical shell subject to a prescribed laterally inhomogeneous heat-flux condition at the outer boundary. Using a numerical model, we explore a broad range of three key dimensionless numbers: a thermal stratification parameter (the relative size of boundary temperature gradients to imposed vertical temperature gradients), $10^{-3} \leqslant S \leqslant 10^{4}$, a buoyancy parameter (the strength of applied boundary heat-flux anomalies), $10^{-2} \leqslant B \leqslant 10^{6}$, and the Ekman number (ratio of viscous to Coriolis forces), $10^{-6} \leqslant E \leqslant 10^{-4}$. We find both steady and time-dependent solutions and delineate the regime boundaries. We focus on steady-state solutions, for which a clear transition is found between a low S regime, in which buoyancy dominates the dynamics, and a high S regime, in which stratification dominates. For the low-S regime, we find that the characteristic flow speed scales as $B^{2/3}$, whereas for high-S, the radial and horizontal velocities scale respectively as $u_r \sim S^{-1}$, $u_h \sim S^{-3/4}B^{1/4}$ and are confined within a thin layer of depth $(SB)^{-1/4}$ at the outer edge of the domain. For the Earth, if lower mantle heterogeneous structure is due principally to chemical anomalies, we estimate that the core is in the high-S regime and steady flows arising from strong outer boundary thermal anomalies cannot penetrate the stable layer. However, if the mantle heterogeneities are due to thermal anomalies and the heat-flux variation is large, the core will be in a low-S regime in which the stable layer is likely penetrated by boundary-driven flows.

Key words: buoyancy-driven instability, rotating flows, stratified flows

1. Introduction

Differential heating at the boundary of a stratified fluid arises in a variety of physical systems. The oceans and atmosphere are heated non-uniformly from above owing to the latitudinal variation of incoming solar energy. Fluid near the

† Email address for correspondence: gracecox@cp.dias.ie

https://doi.org/10.1017/jfm.2018.999 Published online by Cambridge University Press

differentially heated surface moves laterally away from anomalously warm regions towards anomalously cold regions and a significant amount of work has considered whether this 'horizontal convection' can drive large-scale overturning circulations (e.g. Paparella & Young 2002; Siggers, Kerswell & Balmforth 2004; Sheard, Hussam & Tsai 2016; Shishkina 2017). The primary motivation for the present study is differential heating of planetary cores due to lateral heat flow anomalies in their overlying solid mantles. We conduct a systematic investigation of the interaction between thermal stratification and differential boundary heating, incorporating the key ingredients of rapid rotation and spherical shell geometry. Our main focus is to establish the extent to which boundary heat flow anomalies can penetrate and disrupt a pre-existing thermal stratification.

There is now a body of evidence indicating that the cores of Mercury (Christensen 2006), Earth (Davies *et al.* 2015; Nimmo 2015), Mars (Stevenson 2001) and Ganymede (Rückriemen, Breuer & Spohn 2015) are thermally stably stratified below the core–mantle boundary (CMB) owing to a subadiabatic CMB heat flow, with convection (and magnetic field generation) arising at greater depths. The existence of stratification is important because it influences the intensity and structure of the observable magnetic field (Christensen 2006; Stanley & Glatzmaier 2010) and reflects the core's long-term evolution. The strength and thickness of these thermally stable regions is hard to assess due to a lack of direct observations. The stable layer in Earth's core could be up to $\sim$700 km thick (Gubbins *et al.* 2015) with a Brunt–Väisälä frequency comparable to the rotation period. Thermal stratification in the Martian core is usually estimated to have begun around 4 Ga, corresponding to the epoch when the planet lost its global magnetic field (Stevenson 2001), and so the thermally stable region could occupy a significant fraction of the present-day core. Thermal history models for Ganymede predict a stable layer hundreds of kilometres thick (Rückriemen *et al.* 2015).

Terrestrial planetary cores are overlain by rocky mantle, which acts like a viscous fluid convecting on time scales of 10^8 years. In contrast, liquid metal cores have very low viscosity and convect on time scales of 10^3 years. This difference in convection time scales means that the core responds to the CMB as a rigid surface with a fixed heat flux imposed by the lower mantle, whilst the mantle is subjected to a uniform temperature lower boundary condition (Olson & Christensen 2002). Mantle convection simulations produce lateral temperature anomalies of thousands of Kelvin and lateral CMB heat flow variations greater than the mean CMB heat flow (e.g. Nakagawa & Tackley 2008; Olson *et al.* 2015). These lateral variations will inevitably drive baroclinic flows in the underlying core through the thermal wind, but it is unclear the extent to which they will drive penetrative flow within a strongly stratified region.

The competition between stratification and boundary forcing has been explored in some numerical studies of convection in non-magnetic rotating spherical shells, which have shown that thermal boundary anomalies are capable of drastically altering the dynamics compared to uniform thermal boundary conditions (e.g. Zhang & Gubbins 1992, 1993; Gibbons & Gubbins 2000; Gibbons, Gubbins & Zhang 2007). Zhang & Gubbins (1992) solved for steady flows driven by lateral thermal variations at the outer boundary of a rotating spherical shell, having specified temperature rather than heat flux for numerical simplicity. They studied both unstratified and weakly stratified fluids subjected to a range of temperature anomaly patterns and magnitudes. For modest boundary anomaly strengths, patterns of temperature fluctuations and fluid flow lock to the boundary anomaly pattern through the thermal wind, and flows penetrate deep into the shell due to Coriolis effects. Stratification greatly reduces radial

https://doi.org/10.1017/jfm.2018.999 Published online by Cambridge University Press

flow amplitudes, although toroidal flows are less affected, and confine flow towards the outer boundary. The authors speculated that these results would also be obtained in the geophysical case of fixed heat flux boundary anomalies. Gibbons & Gubbins (2000) were able to confirm this for steady flows in their subsequent investigation of weakly stratified fluids in rotating spherical shells. They applied different spatial distributions and magnitudes of large-scale boundary heat flow anomalies to fluids of varying stratification strengths. For equatorially symmetric patterns, rotational effects dominate the dynamics at weak or no stratification. As the stratification increases, rotational effects become less important, radial flow diminishes and flow is confined to a layer beneath the outer boundary. Smaller length scale heat-flux patterns drive less energetic flows that are not able to penetrate as deeply into the fluid. Solutions become increasingly smaller scale with increasing boundary anomaly magnitude, with correspondingly higher computational expense. Gibbons & Gubbins (2000) suggested that solutions would become unstable (time dependent) with sufficiently strong boundary anomalies, although computational limitations prevented the authors from identifying the parameters at which this occurs.

Several authors have considered the more realistic but more complex magnetohydrodynamic (MHD) case by studying numerical simulations of dynamos in partially stratified spherical shells, including Christensen (2006), Christensen & Wicht (2008), Stanley & Mohammadi (2008), Aurnou & Aubert (2011), Nakagawa (2011), Nakagawa (2015) and Olson, Landeau & Reynolds (2017). Some numerical models have shown that the presence of a stable layer fundamentally changes dynamo action and can drastically alter the magnetic field at the planetary surface compared to equivalent models with no stable layer. For example, Christensen (2006) showed that a strong magnetic field at the top of the dynamo generating region diffuses through a stable layer such that the small scale, rapidly varying components are filtered out.

Dynamo models with heterogeneous thermal boundary conditions have also been investigated by various authors, see the review by Amit *et al.* (2015) and references therein. As in the non-magnetic case, within MHD models heterogeneous boundary forcing has been shown to have a significant effect, for example by modifying the morphology of the magnetic field (e.g. Olson & Christensen 2002; Gubbins, Willis & Sreenivasan 2007; Aurnou & Aubert 2011) such that its long-term fundamental symmetries follow the spatial symmetries of the imposed heat-flux pattern, or by locking the magnetic field to regions of anomalously high heat flow (Willis, Sreenivasan & Gubbins 2007; Sreenivasan 2009). In some circumstances, strong boundary-driven flows can also overwhelm the convection such that dynamo action is weakened or destroyed altogether (Olson & Christensen 2002; Takahashi *et al.* 2008). Although ultimately the most physically relevant model, a thorough scaling analysis of the competition between stratification and boundary forcing within an MHD setting is beyond what is currently achievable. Some progress has been made by studying weakly stratified models with heterogeneous outer boundary conditions (e.g. Sreenivasan & Gubbins 2008; Aurnou & Aubert 2011; Olson *et al.* 2017), although the extrapolation gap from the parameters used in these models to realistic values is large.

This work focusses on the simpler, non-magnetic problem which is yet not fully described. In particular, the previous studies described above have been limited to highly viscous, weakly stratified fluids in spherical shells with moderate rotation rates and subject to relatively weak boundary anomalies: it is not clear how these results bear on the rapidly rotating, strongly stratified case relevant to planetary cores that are additionally subject to significant lateral variations in heat flux at

https://doi.org/10.1017/jfm.2018.999 Published online by Cambridge University Press

their outer boundary. One severe computational limitation that has hampered progress arises because rotating flows adopt small azimuthal length scales even at the onset of convection (Chandrasekhar 1961), while increasing the amplitude of the driving force generates a broad spectrum of flow structures that become increasingly difficult to resolve. In this study, we minimise this problem by considering a subset of steady-state solutions obtained from solving the full time-dependent equations, and also by assuming that the entire fluid domain is stably stratified without any internal heat sources that drive internal convection. This is equivalent to assuming that any underlying convection does not significantly penetrate or mix an overlying stable region, which is true in the case of strong stratification (Takehiro & Lister 2001; Buffett & Seagle 2010; Gubbins & Davies 2013). These assumptions allow us to isolate the interaction between outer boundary forcing and pre-existing stratification, without the additional complication of destabilisation of stratified fluid from below by internal convection, and to study the dynamics using a much wider range of parameters than has been possible previously.

The fluid dynamical problem we consider depends upon three dimensionless numbers (detailed definitions are given in 2.1): a thermal stratification parameter, S, defined as the relative size of boundary temperature gradients to imposed vertical temperature gradients, a buoyancy parameter, B, measuring the strength of the applied boundary heat-flux anomalies, and the Ekman number, E, the ratio of viscous and Coriolis forces. Our study spans the ranges $10^{-2} \leqslant B \leqslant 10^{6}$, $10^{-3} \leqslant S \leqslant 10^{4}$ and $10^{-6} \leqslant E \leqslant 10^{-4}$. We focus primarily on the case where the aspect ratio, the ratio of inner to outer boundary radii, corresponds to that of Earth's liquid core, $r_i/r_o = \eta = 0.35$. Additional simulations are performed at $\eta = 0.01$, which is almost a full sphere and approximates the core geometry of Mars and Ganymede.

For each choice of (E, S, B) a heat flow pattern must be chosen. Previous studies clearly show that the influence of thermal boundary anomalies on the structure and dynamics of rotating fluids becomes more pronounced as the length scale of the imposed pattern is increased (Zhang & Gubbins 1992, 1993; Davies, Gubbins & Jimack 2009). We choose to apply a Y_2^2 spherical harmonic boundary heat flow pattern since this the largest component of shear-wave variation (a likely proxy for CMB heat flow) in Earth's lower mantle (Dziewonski, Lekic & Romanowicz 2010); it is also a common boundary condition of previous studies, which makes comparison straightforward (e.g. Zhang & Gubbins 1992, 1993; Davies *et al.* 2009; Sreenivasan 2009; Sahoo & Sreenivasan 2017).

We have conducted a suite of 99 numerical simulations finding predominantly steady solutions, which partition into two distinct regimes. Within each regime we formulate theoretical scaling laws that provide excellent fits to our dataset and permit extrapolation to the parameter regimes appropriate to planetary interiors. The remainder of the paper is structured as follows: the mathematical formulation is given in § 2, results of the numerical simulations are presented in § 3, scaling analyses and their application to Earth and Ganymede's outer cores follow in §§ 4 and 5 and a summary of results is found in § 6.

2. Method

We consider an incompressible Boussinesq fluid in an impenetrable spherical shell, of outer radius r_o and inner radius r_i, rotating about the axial $\hat{z}$ direction with constant angular velocity Ω. The whole shell is thermally stratified and compositional effects are neglected, as in Gibbons & Gubbins (2000), in order to isolate the effects of

https://doi.org/10.1017/jfm.2018.999 Published online by Cambridge University Press

thermal boundary anomalies on a thermally stratified fluid. Again following Gibbons & Gubbins (2000), we also neglect the magnetic field so as to reach more realistic E, B and S values; the effects of free convection and the resulting magnetic field evolution will be investigated in a future study. In the following work, r, θ and ϕ denote spherical polar coordinates, $\boldsymbol{r}$ is the position vector and t is time.

2.1. *Governing equations and non-dimensionalisation*

Following the formulation of Zhang & Gubbins (1992) and Gibbons & Gubbins (2000), the temperature is split into a steady radial part, T_0, and a time-varying part, T_1, such that

$$T(r, \theta, \phi, t) = T_0(r) + T_1(r, \theta, \phi, t). \tag{2.1}$$

The steady radial temperature profile satisfies

$$\kappa \nabla^2 T_0 = F, \tag{2.2}$$

where κ is the thermal diffusivity and $F \geqslant 0$ is a heat sink that is chosen to impose a background thermal gradient that, if strong, suppresses radial motion. Integrating with respect to r in spherical coordinates gives

$$r^2 \frac{\mathrm{d}T_0}{\mathrm{d}r} = \beta r^3 + A, \tag{2.3}$$

where $\beta = F/3\kappa$ and A is a constant of integration. Setting the outer boundary condition such that

$$\left.\frac{\mathrm{d}T_0}{\mathrm{d}r}\right|_{r=r_o} = \beta r_o \tag{2.4}$$

results in $A = 0$ and so within the spherical shell $\mathrm{d}T_0/\mathrm{d}r = \beta r$.

We define the outer boundary condition of the temperature gradient as

$$\left.\frac{\partial T_1}{\partial r}\right|_{r=r_o} = \mathcal{H} Y_2^2(\theta, \phi), \tag{2.5}$$

in which the spatial pattern of the anomaly is given by the spherical harmonic $Y_2^2(\theta, \phi)$, and the magnitude of the anomaly is given by $\mathcal{H}$. Rewriting the general temperature equation

$$\frac{\partial T}{\partial t} + (\boldsymbol{u} \cdot \nabla) T = \kappa \nabla^2 T - F, \tag{2.6}$$

using (2.1) and (2.4) leaves

$$\frac{\partial T_1}{\partial t} + (\boldsymbol{u} \cdot \nabla) T_1 + u_r \beta r = \kappa \nabla^2 T_1 \tag{2.7}$$

as the temperature equation.

The equations for conservation of momentum in a rotating frame of reference and for conservation of mass are

$$\frac{\partial \boldsymbol{u}}{\partial t} + (\boldsymbol{u} \cdot \nabla)\boldsymbol{u} + 2\Omega(\hat{\boldsymbol{z}} \times \boldsymbol{u}) = -\nabla\left(\frac{P'}{\rho_0}\right) + \frac{\rho' \boldsymbol{g}}{\rho_0} + \nu \nabla^2 \boldsymbol{u} \tag{2.8}$$

https://doi.org/10.1017/jfm.2018.999 Published online by Cambridge University Press

and

$$\boldsymbol{\nabla}\cdot\boldsymbol{u}=0, \tag{2.9}$$

where $\boldsymbol{u}$ is velocity, P' is the pressure perturbation, ρ_0 is a reference density, ρ' is the deviation from the reference density, $\boldsymbol{g}$ is gravity and ν is the kinematic viscosity. Expressing ρ' as

$$\rho'=-\rho_0\alpha_T T_1, \tag{2.10}$$

where α_T is the coefficient of thermal expansivity, gives an alternative form of the momentum equation

$$\frac{\partial\boldsymbol{u}}{\partial t}+(\boldsymbol{u}\cdot\boldsymbol{\nabla})\boldsymbol{u}+2\Omega(\hat{\boldsymbol{z}}\times\boldsymbol{u})=-\boldsymbol{\nabla}\hat{P}+\alpha_T\gamma T_1\boldsymbol{r}+\nu\nabla^2\boldsymbol{u}, \tag{2.11}$$

where $\hat{P}$ is the reduced pressure ($=P'/\rho_0$) and γ is a constant ($\boldsymbol{g}=-\gamma\boldsymbol{r}$).

Scaling radius by a characteristic length scale d ($=r_o-r_i$), time by the thermal diffusion time d^2/κ, velocity by κ/d and temperature by $\mathcal{H}d$ (from (2.5)) gives the radial temperature profile and the temperature and momentum equations in their dimensionless forms

$$\frac{\mathrm{d}T_0^*}{\mathrm{d}r^*}=Sr^*, \tag{2.12}$$

$$\frac{\partial T_1^*}{\partial t^*}+(\boldsymbol{u}^*\cdot\boldsymbol{\nabla})T_1^*+Su_r^*r^*=\nabla^2T_1^* \tag{2.13}$$

and

$$\frac{E}{Pr}\left[\frac{\partial\boldsymbol{u}^*}{\partial t^*}+(\boldsymbol{u}^*\cdot\boldsymbol{\nabla})\boldsymbol{u}^*\right]+(\hat{\boldsymbol{z}}^*\times\boldsymbol{u}^*)=-\boldsymbol{\nabla}\hat{P}+BT_1^*\boldsymbol{r}^*+E\nabla^2\boldsymbol{u}^*, \tag{2.14}$$

where $\boldsymbol{r}^*$ is the dimensionless radial vector, S is the stratification parameter, E is the Ekman number, Pr is the Prandtl number and B is the buoyancy parameter. These dimensionless numbers are defined as

$$S=\frac{\beta d}{\mathcal{H}},\quad E=\frac{\nu}{2\Omega d^2},\quad Pr=\frac{\nu}{\kappa},\quad B=\frac{\alpha_T\gamma\mathcal{H}d^3}{2\Omega\kappa}, \tag{2.15a–d}$$

and B is related to E and a Rayleigh number, $Ra_{\mathcal{H}}$, where

$$\frac{B}{E}=Ra_{\mathcal{H}}=\frac{\alpha_T\gamma\mathcal{H}d^5}{\nu\kappa}. \tag{2.16}$$

In this work, all calculations are performed at $Pr=1$ for numerical convenience and the majority with a shell aspect ratio $\eta=0.35$; a summary of model parameters is given in tables 3–6 in appendix A. We investigate the effects of varying the shell aspect ratio using models with $\eta=0.01$ in § 4.3. The governing equations are solved for $\boldsymbol{u}$ and T_1 with no-slip boundary conditions on both inner and outer boundaries, a fixed temperature of zero imposed on the inner boundary and a fixed heat flux imposed on the outer boundary, as previously discussed. A detailed description of the pseudo-spectral code may be found in Willis *et al.* (2007) and Davies, Gubbins & Jimack (2011), and in the most recent dynamo benchmark paper (Matsui *et al.* 2016). Although (2.1)–(2.5) give the clearest mathematical description of our method, in fact the code solves the following equation

$$\frac{\partial T^*}{\partial t^*}+(\boldsymbol{u}^*\cdot\boldsymbol{\nabla})T^*=\nabla^2T^*-3S, \tag{2.17}$$

https://doi.org/10.1017/jfm.2018.999 Published online by Cambridge University Press

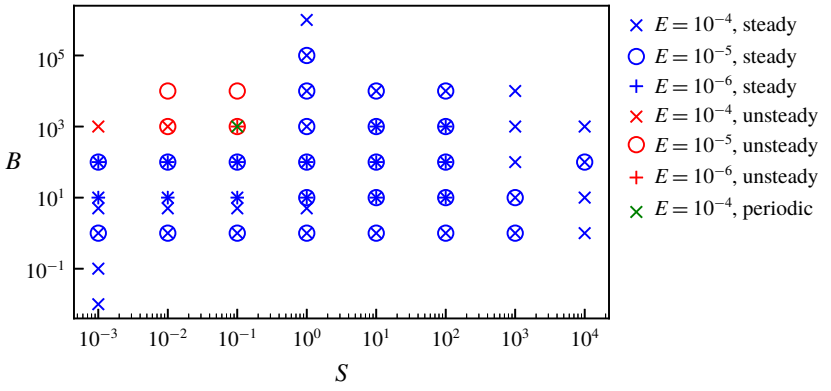


FIGURE 1. (Colour online) Stability diagram in (S, B) parameter space showing all models summarised in tables 3–5. The symbol type represents the Ekman number (crosses denote $E = 10^{-4}$, circles denote $E = 10^{-5}$ and plus signs denote $E = 10^{-6}$); the symbol colour represents the stability of the solution obtained (blue denotes a steady-state solution, red denotes a time-dependent solution and green denotes a periodic solution).

which is equivalent to (2.13). To benchmark our code for this particular problem, we reproduced the flow magnitudes and spatial patterns reported in Gibbons & Gubbins (2000), using a shell aspect ratio $\eta = 0.4$ and their parameters of $E = 10^{-3}$, $Pr = 1$, $B = 1$ and $S = 0$ and $S = 100$.

Given that we focus upon steady-state solutions to the time-dependent equations, for numerical expediency where possible we used the final steady-state solution of a model nearby in parameter space as the initial condition. Models were run long past the initial transient period and until the volume-averaged kinetic energy converged to a steady value. Several numerical models were unstable and no steady-state solutions were obtained at those parameters. In such cases, we cannot rule out the existence of a steady-state model using different initial conditions.

For each of our models, spatial convergence was verified by assessing the kinetic energy power spectrum as a function of spherical harmonic degree (l) and order (m). For all models, the maximum power was found at long wavelengths (the lowest l), which generally exceeded the power in the shortest wavelengths (high l) by a large amount: at least two, although usually four or five, orders of magnitude.

Figure 1 is a stability diagram showing regions of parameter space resulting in steady and unsteady solutions. The figure shows the transition between high B and low S models, which are unsteady, and higher S models, which produce a steady state. One periodic model was obtained at the boundary between the steady and unsteady regions of parameter space. In the remainder of this work, we focus our attention upon the steady-state regime; time-dependent models are the subject of a future paper.

3. Results

Figure 2 shows the temperature perturbations in the equatorial plane, denoted T_f^*, for models at $E = 10^{-4}$ and a range of B and S values. Note that in the remainder of this text, we use T_f^* (the fluctuating part of the temperature) as a proxy for T_1^* defined in (2.1). To calculate the quantity T_f^*, the Y_0^0 spherical harmonic component of the total temperature T^* has been removed, which includes all of T_0^* and also the mean of T_1^*. Therefore, T_f^* and T_1^* differ in that the former is zero mean and the

https://doi.org/10.1017/jfm.2018.999 Published online by Cambridge University Press

latter is not. Figures 3 and 4 show the radial and azimuthal velocity components, u_r^* and u_ϕ^*, for the same models. At low B and S, the temperature fluctuations are large scale with a Y_2^2 spatial pattern locked to the applied heat-flux pattern on the outer boundary and penetrating through the whole shell depth. The two lobes of negative temperature (blue) correspond to regions of high outward heat flux and the two lobes of positive temperature (red) correspond to regions of low outward heat flux. Zeroes of T_f^* (at $\phi \approx \pi/4, 3\pi/4, 5\pi/4, 7\pi/4$) correspond to locations of the outer boundary heat flux changing sign. The radial velocity is dominated by large-scale convection cells that occupy the whole shell, with two upwellings and two downwellings present, and the peak velocity amplitudes occur at approximately half the shell radius. The lateral locations of these maxima and minima approximately correspond to locations of $T_f^* = 0$. In azimuthal velocity, locations of diverging (converging) lobes of opposite sign correspond to locations of upwellings (downwellings) of radial flow and $T_f^* = 0$.

As the stratification parameter (S) increases, temperature perturbations and flow magnitudes decrease and the dynamics becomes concentrated towards the outer boundary rather than occupying the entire shell thickness. Radial flow cells begin to elongate near the inner boundary, and high velocity magnitudes are concentrated near the outer boundary rather than the inner boundary. In u_ϕ^*, inner and outer cells of the same polarity begin to join together through tails trailing from the outermost cells, with the inner cells decreasing in amplitude. Radial flow is strongly suppressed with increasing S, which is expected because stratification does not permit large radial velocities. Azimuthal flow is only weakly suppressed with increasing stratification as horizontal flows are permitted within a stably stratified layer. At high S, all flow becomes confined to a thin shear layer of thickness δ^* beneath the outer boundary (hereafter referred to as the 'penetration depth' into the fluid).

As B increases, temperature perturbations decrease and flow magnitudes increase. This is a consequence of the fixed heat-flux outer boundary condition; increasing the buoyancy produces stronger flows that better homogenise the temperature, resulting in velocity increasing with B while temperature perturbations decrease (e.g. Otero *et al.* 2002; Mound & Davies 2017). Flows are phase shifted so that upwellings (and diverging u_ϕ^*) and downwellings (and converging u_ϕ^*) are now locked to the boundary pattern itself rather to locations of heat flux changing sign. Upwellings (downwellings) are beneath high (low) boundary heat flow regions. At low S and increasing B (e.g. figures 2–4(*a–c*)), temperature and flow patterns are strikingly different from models at other parameters. Downwellings become increasingly faster and much narrower in azimuth with increasing B, although still occupying the whole shell radius, whilst the upwellings remain broad and low amplitude. This pattern of slow, broad upwellings and fast, narrow downwellings in the presence of lateral boundary anomalies was also obtained in e.g. Willis *et al.* (2007), Sreenivasan & Gubbins (2011). At higher S, upwellings and downwellings are of similar lateral extent and the dynamics is confined to a thin shear layer whose thickness decreases with increasing S and B.

Figure 5 shows u_r^* (*a*,*d*,*g*,*j*) and u_ϕ^* (*b*,*e*,*h*,*k*) and T_f^* (*c*,*f*,*i*,*l*) in a meridional plane for models run at $E = 10^{-4}$ and $B = 1$ for a range of stratification parameters (S). At low S, the dynamics is dominated by large-scale features that are aligned with the rotation axis. There is little variation parallel to the z-axis, as expected in a rapidly rotating system from the Taylor–Proudman theorem. As stratification increases, the dynamics is confined to the shear layer at the top of the shell, as seen in figures 2–4, which means that significant z variations now occur in the models of the order of the penetration depth, δ^*.

https://doi.org/10.1017/jfm.2018.999 Published online by Cambridge University Press

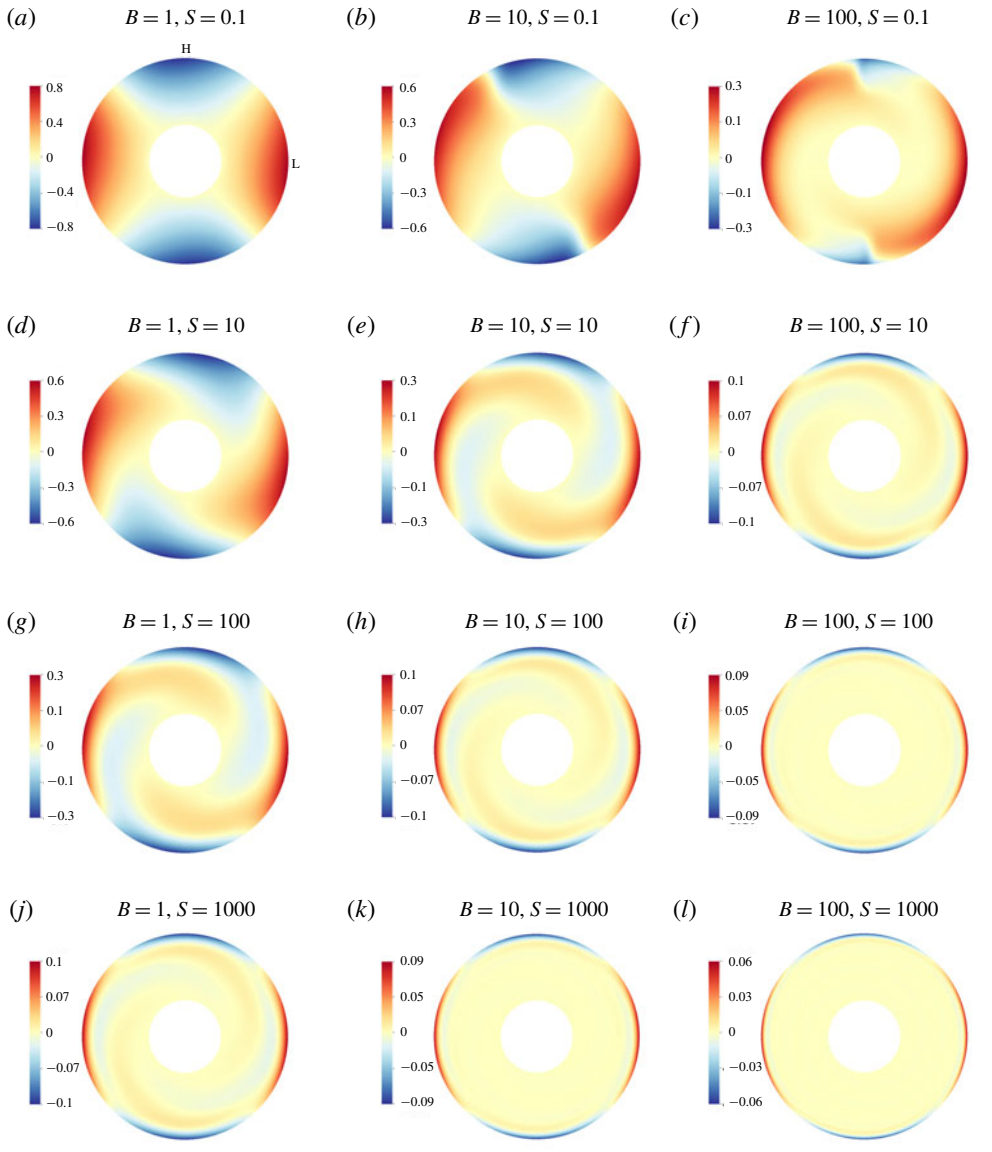


FIGURE 2. (Colour online) Equatorial plots of T_f^* for models at $E = 10^{-4}$ and varying S (increasing from top to bottom) and B (increasing from left to right). Red indicates positive values and blue indicates negative values. Note the different colour scales. Locations of high (H) and low (L) outward heat flux are shown on (*a*).

Figure 6 shows $\langle u_r^* \rangle_v$, $\langle u_\phi^* \rangle_v$, $\langle v_\theta^* \rangle_v$ and $\langle T_f^* \rangle_v$, where the angular brackets denote the magnitude averaged over the shell volume V such that, for example, $\langle u_r^* \rangle_v = \int |u_r^*| \, \mathrm{d}V$, and likewise for vector quantities. We define a similar operator for the integral over a surface S of radius r such that $\langle u_r^* \rangle_s = (1/S) \int |u_r^*| \, \mathrm{d}S$. We adopt an average over the entire domain, rather than only the shear layer volume, because it is difficult to estimate the exact location of the shear layer edge. We assume that the quantities of interest are dominated by their values within the shear layer, with negligible contribution from elsewhere in the domain, such that our volume-averaged

https://doi.org/10.1017/jfm.2018.999 Published online by Cambridge University Press

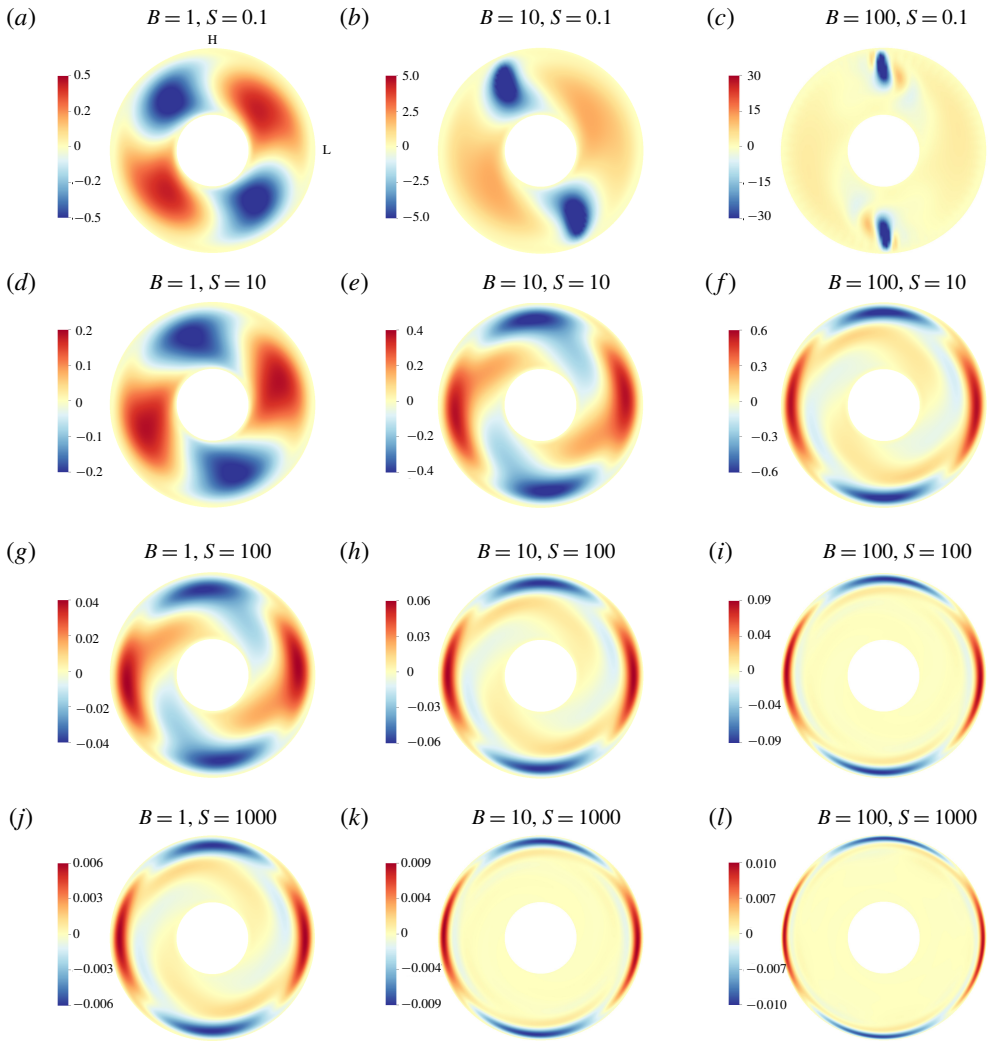


FIGURE 3. (Colour online) Equatorial plots of u_r^* for models at $E = 10^{-4}$ and varying S (increasing from top to bottom) and B (increasing from left to right). Red indicates positive values and blue indicates negative values. Note the different colour scales. Locations of high (H) and low (L) outward heat flux are shown on (*a*).

quantities are representative of the shear layer volume average. Furthermore, we use the average of the modulus because integration over solid angle would otherwise result in large-scale cancellation due to the spherical symmetry of the problem. The volume-averaged quantities show a clear transition from the low stratification (S) regime, in which the dynamics appears to be related to B and E only, and the high S regime, in which stratification dominates the dynamics and the quantities obey power law relationships in both S and B.

We use the location of the peak in $\langle u_r^* \rangle_s$ as a function of radius to estimate the penetration depth, δ^*, for each model. We define the radius of maximum $\langle u_r^* \rangle_s$ as r_{max}

https://doi.org/10.1017/jfm.2018.999 Published online by Cambridge University Press

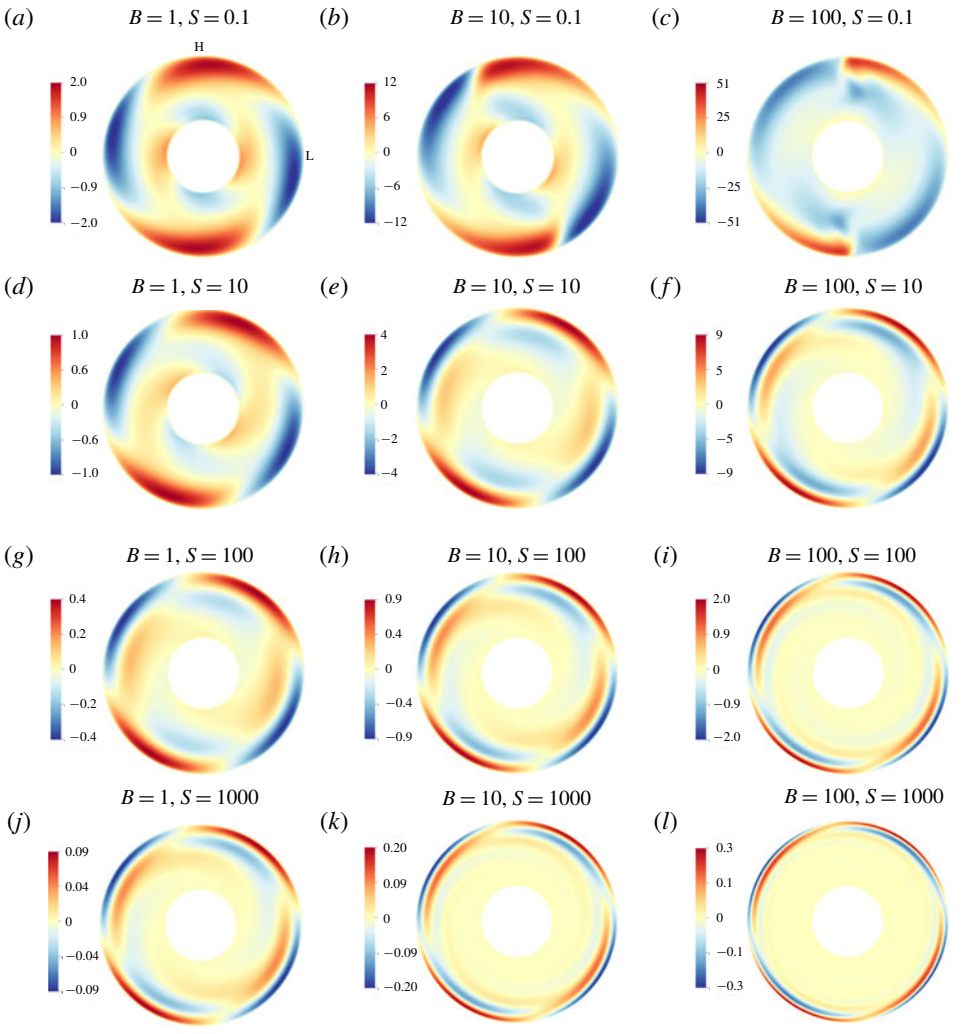


FIGURE 4. (Colour online) Equatorial plots of u_ϕ^* for models at $E = 10^{-4}$ and varying S (increasing from top to bottom) and B (increasing from left to right). Red indicates positive values and blue indicates negative values. Note the different colour scales. Locations of high (H) and low (L) outward heat flux are shown on (*a*).

and calculate the penetration depth as follows

$$\delta^* = r_o - r_{max}. \tag{3.1}$$

Radial velocity is used to estimate the penetration depth because it has only a single peak that is located centrally within the shear layer, whereas the horizontal components typically have several peaks, with the highest value close to the outer boundary in our $S > 1$ models (see the equatorial sections in figures 3 and 4, and figure 7 for a representative example of radial velocity profiles). Note that the $\langle\rangle_s$ operation averages any longitudinal dependence of u_r^*, as seen in figure 5 for example. Figure 8 shows that δ^* has different behaviour in the two stratification (S) regimes, with δ^* of the order of the shell thickness at low S and obeying power law relationships in S and B.

https://doi.org/10.1017/jfm.2018.999 Published online by Cambridge University Press

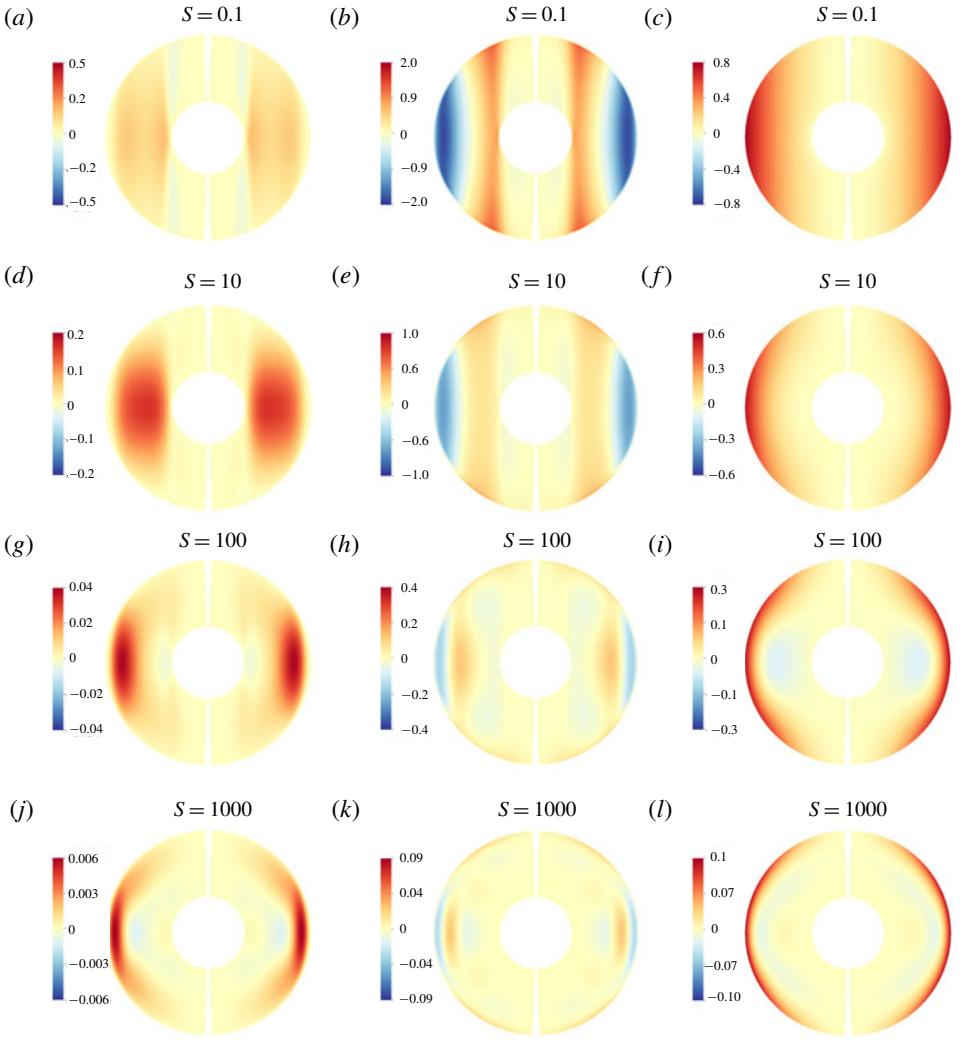


FIGURE 5. (Colour online) Meridional plots of u_r^* (*a*,*d*,*g*,*j*), u_θ^* (*b*,*e*,*h*,*k*) and T_f^* (*c*,*f*,*i*,*l*) for models at $E = 10^{-4}$, $B = 1$ and varying S (increasing from top to bottom). Red indicates positive values and blue indicates negative values.

4. Scaling analysis

In this section, our aim is to recover power laws of the form

$$f = S^a B^b \tag{4.1}$$

from the governing equations to express the velocity components, temperature fluctuations and penetration depth (denoted f above) as functions of the control parameters S and B (and, equivalently, S, $Ra_{\mathcal{H}}$ and E), where coefficients a and b are to be determined. We then verify these predicted scalings for our models using the volume-averaged quantities introduced above, and finally we extrapolate the power laws to planetary core conditions.

https://doi.org/10.1017/jfm.2018.999 Published online by Cambridge University Press

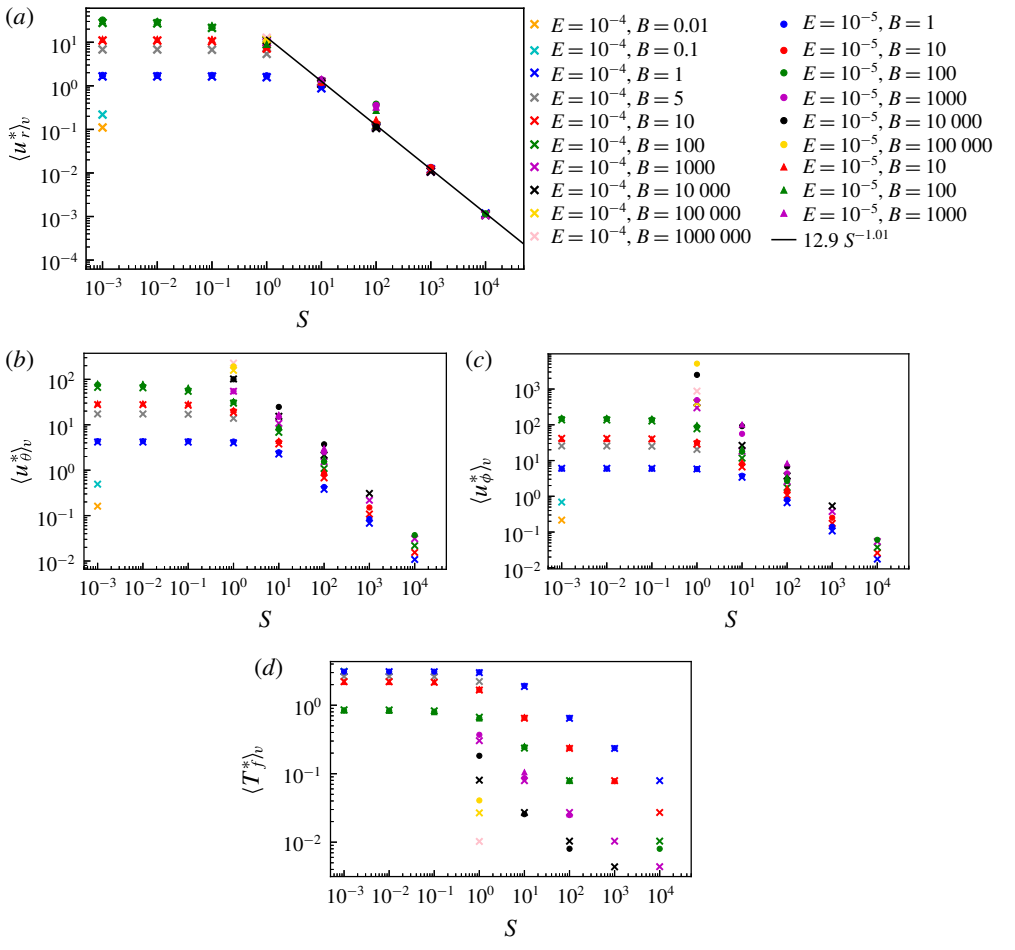


FIGURE 6. (Colour online) Volume-averaged values of the absolute (*a*) radial velocity, $\langle u_r^* \rangle_v$, (*b*) meridional velocity, $\langle u_\theta^* \rangle_v$, (*c*) azimuthal velocity, $\langle u_\phi^* \rangle_v$ and (*d*) temperature perturbations, $\langle T_f^* \rangle_v$, as a function of the stratification parameter, S, for all steady models. Symbol shapes represent the Ekman number, E, and colours represent the buoyancy parameter, B. The black line in panel (*a*) is the power law best fit for all models at $S > 1$.

4.1. *High stratification regime*

At high stratification parameter, S, flow is confined to a shear layer of thickness δ^* at the top of the shell and this penetration depth decreases with increasing stratification. Within the layer, flow tends to be in long, thin lobes with relatively little lateral variation, which suggests that the radial gradients of velocity ($\partial/\partial r^*$) are larger than the horizontal ($\partial/\partial\theta^*$ and $\partial/\partial\phi^*$) gradients. Our dimensionless horizontal lengths are $O(1)$ and the relevant radial length scale is $O(\delta^*)$ so that the continuity equation (2.9) gives a relationship between the velocity components

$$u_r^* \sim \delta^* u_\theta^* \sim \delta^* u_\phi^*, \tag{4.2}$$

assuming that $\partial/\partial\theta^* \sim \partial/\partial\phi^*$. Adherence of our high S models to this scaling was verified using the estimates of δ^* shown in figure 8 and volume-averaged velocities

https://doi.org/10.1017/jfm.2018.999 Published online by Cambridge University Press

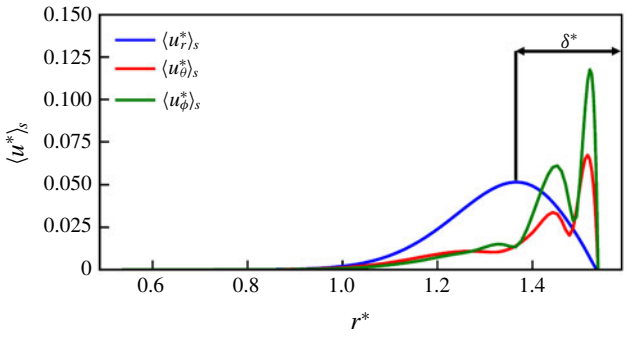


FIGURE 7. (Colour online) Components of velocity as a function of radius for a model run at $E = 10^{-4}$, $B = 100$ and $S = 1000$. The line colour denotes the flow component (blue for radial, red for meridional and green for azimuthal). The black arrow represents the width used as an estimate for the penetration depth, δ^*, in this model (calculated according to (3.1)).

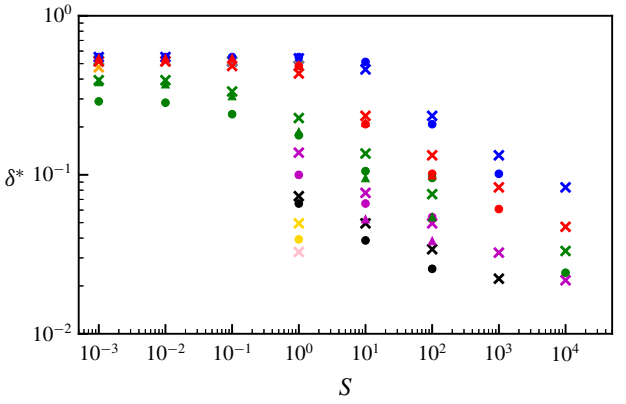


FIGURE 8. (Colour online) Estimates of the penetration depth δ^*, as a function of the stratification parameter, S, for all steady models. Symbol shapes represent the Ekman number, E, and colours represent the buoyancy parameter, B. The key is given in figure 6(*a*).

$\langle u^*_r\rangle_v$, $\langle u^*_\theta\rangle_v$ and $\langle u^*_\phi\rangle_v$ shown in figure 6. These results, summarised in figure 14 in appendix B, show clear flattening of $\langle u^*_r\rangle_v/\delta^*\langle u^*_h\rangle_v$ for the highest S models, where $\langle u^*_h\rangle_v$ is the average volume-averaged horizontal velocity ($= [\langle u^*_\theta\rangle_v + \langle u^*_\phi\rangle_v]/2$).

4.1.1. *Vorticity equation balance*

Taking the curl of (2.14) gives the dimensionless vorticity equation for steady flow

$$\frac{\partial \boldsymbol{u}^*}{\partial z^*} = \boldsymbol{\nabla} \times BT_1^* \boldsymbol{r}^* + E\nabla^2 \boldsymbol{\omega}^*, \tag{4.3}$$

in which pressure does not appear and inertia is assumed small. In this three-term balance, we note that the buoyancy term is purely horizontal, and so the radial component of the first term must be small except outside the viscous boundary layer. Motivated by the observation that the viscous term is large only near the boundaries (see figure 15 in appendix B), we seek a thermal wind balance between the horizontal

https://doi.org/10.1017/jfm.2018.999 Published online by Cambridge University Press

components of the Coriolis and buoyancy terms, and will show subsequently that the resulting scaling remains consistent for cases in which viscosity is also included in the balance.

We adopt δ^* as the relevant length scale in the Coriolis term that controls variations parallel to the rotation axis at high stratification (see figure 5), and an $O(1)$ horizontal length scale for the buoyancy term since it is determined by the boundary condition. The balance is then

$$\frac{u^*_{\theta,\phi}}{\delta^*} \sim BT^*_1. \tag{4.4}$$

The volume-averaged magnitude of the Coriolis and buoyancy terms, scaled by our approximations to those terms using δ^* and volume-averaged velocities and temperatures ($\partial \boldsymbol{u}^*/\partial z^* \sim \langle u^* \rangle_v/\delta^*$ for Coriolis and $\boldsymbol{\nabla} \times BT^*_1 \boldsymbol{r}^* \sim B\langle T^*_f \rangle_v$ for buoyancy), are plotted for all models in figures 16 and 17 in appendix B. These ratios are approximately one for all high S models, and show little S dependence, indicating that the correct scalings are encapsulated in our approximations and that the volume-averaged quantities are suitable diagnostics of model output.

4.1.2. *Temperature equation balance*

The dimensionless time-independent temperature equation is

$$\nabla^2 T^*_1 - u^*_r \frac{\partial T^*_1}{\partial r^*} - \frac{u^*_\theta}{r}\frac{\partial T^*_1}{\partial \theta} - \frac{u^*_\phi}{r \sin\theta}\frac{\partial T^*_1}{\partial \phi} - S u^*_r r^* = 0. \tag{4.5}$$

Assuming that diffusion occurs on the length scale of the penetration depth, and that the geometric factors of r and $\sin\theta$ are order unity, leaves

$$\frac{T^*_1}{\delta^{*2}} - 3\frac{u^*_r}{\delta^*} T^*_1 - S u^*_r \approx 0 \tag{4.6}$$

using the scaling for the velocity components of (4.2). The term $(\boldsymbol{u}^* \cdot \boldsymbol{\nabla}) T^*_1$ is small compared to the other terms (see figure 18 in appendix B for two representative high S models). Therefore,

$$\frac{T^*_1}{\delta^{*2}} \sim S u^*_r \tag{4.7}$$

is the appropriate balance. The approximation $\nabla^2 T^*_1 \sim \langle T^*_f \rangle_v/\delta^{*2}$ and the term balance in the temperature equation described by (4.7) were verified for our high S models (see figure 19 in appendix B, which shows a clear flattening of $(\langle T^*_f \rangle_v/\delta^{*2})/S\langle u^*_r \rangle_v$ for higher stratification parameters and little dependence on B).

4.1.3. *Power law scalings*

Rearranging (4.7) for δ^*, eliminating u^*_r using (4.2) from the continuity equation and substituting $BT^*_1\delta^*$ for horizontal flow (from balancing $\partial \boldsymbol{u}^*/\partial z^*$ with $\boldsymbol{\nabla} \times BT^*_1 \boldsymbol{r}^*$ in (4.3)), results in a scaling for the penetration depth in terms of the control parameters

$$\delta^* \sim (SB)^{-1/4} \sim (SRa_{\mathcal{H}}E)^{-1/4}. \tag{4.8}$$

We now postulate that the radial velocity u^*_r depends on S but not B as it is not directly forced by the thermal wind; it arises to conserve mass for the horizontal velocity components, which are directly forced by the boundary anomalies. Then

$$u^*_r \sim S^a, \tag{4.9}$$

https://doi.org/10.1017/jfm.2018.999 Published online by Cambridge University Press

and the horizontal flow components scale as

$$u^*_{\theta,\phi} \sim S^{a+1/4} B^{1/4}, \tag{4.10}$$

from (4.2). The temperature perturbations depend on both S and B

$$T^*_1 \sim S^b B^c, \tag{4.11}$$

where the exponents b and c are to be determined. From (4.7) and (4.8),

$$S^{b-a} B^c \sim \frac{T^*_1}{u^*_r} \sim \delta^{*2} S \sim S^{1/2} B^{-1/2}, \tag{4.12}$$

substituting (4.9) and (4.11), from which we deduce $c = -1/2$ and $b - a = 1/2$. Another assumption is required in order to proceed further with the analysis. We now assume that at sufficiently high β, the boundary anomalies become unimportant so that the temperature perturbations are independent of $\mathcal{H}$. Then, T^*_1 can only depend on the product SB and, since the power of B is $-1/2$, the power of S $(= b)$ must also be $-1/2$. We have now determined the exponents for the temperature fluctuations

$$T^*_1 \sim (SB)^{-1/2} \sim (SRa_{\mathcal{H}} E)^{-1/2}, \tag{4.13}$$

radial flow

$$u^*_r \sim S^{-1}, \tag{4.14}$$

and horizontal flow components

$$u^*_{\theta,\phi} \sim S^{-3/4} B^{1/4} \sim S^{-3/4} Ra^{1/4}_{\mathcal{H}} E^{1/4}. \tag{4.15}$$

4.1.4. *Empirical fit to models*

In order to test the scaling laws obtained in the previous section, we computed best fits to our models using a least squares inversion of the estimates of the penetration depth and the volume-averaged velocities and temperature perturbations. We seek power laws of the form

$$\tilde{y} = \epsilon S^\chi B^\zeta, \tag{4.16}$$

where the 'observations' y are model outputs, and the predictions $\tilde{y}$ are calculated from the control parameters S and B, given the specified functional form. We take the logarithm to transform the power law problem into a linear problem such that

$$\log \tilde{y} = \log \epsilon + \chi \log S + \zeta \log B \tag{4.17}$$

and calculate the prefactor ϵ and exponents χ and ζ using a linear least squares inversion. A summary of the predicted scaling exponents ((4.8) and (4.13)–(4.15)) and those obtained from the least squares fits to all models in the stratification-dominated regime ($S > 1$) is provided in table 1 for comparison. A measure of how well the models are fit is given by the R^2 values (rounded to two decimal places throughout). The best fitting exponents are in good agreement with those obtained in the analysis; see also figures 9(*a*)–9(*c*).

4.1.5. *The role of viscosity*

Having verified our two-term balance in the vorticity equation, we now address the question of whether our scalings are also consistent when considering all three terms.

https://doi.org/10.1017/jfm.2018.999 Published online by Cambridge University Press

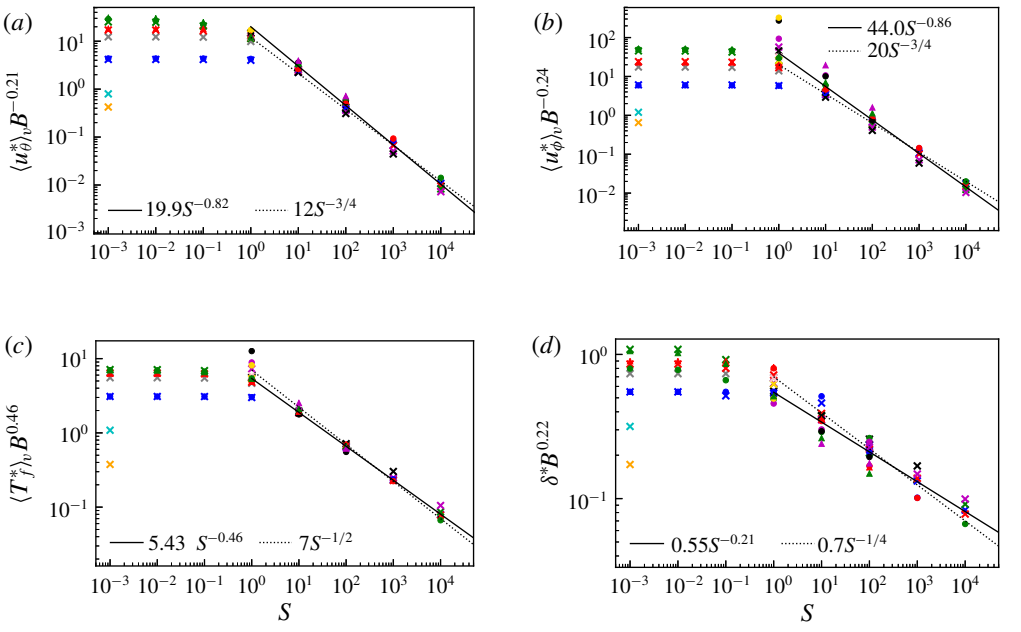


FIGURE 9. (Colour online) (*a*) Volume-averaged meridional velocities, (*b*) volume-averaged azimuthal velocities, (*c*) volume-averaged temperature perturbations and (*d*) penetration depth estimates, normalised by the best empirical fit to the buoyancy parameter for all models with $S > 1$, as a function of S. Symbol shapes represent the Ekman number, E, and colours represent the buoyancy parameter, B. The key is given in figure 6(*a*). The solid black lines show the best fitting power laws for S in the stratification-dominated regime and the dotted lines show the theoretically predicted S exponents.

Quantity	Prediction	Fit to models	Fit R^2
u_r^*	S^{-1}	$S^{-1.01}B^{0.02}$	0.98
u_ϕ^*	$S^{-3/4}B^{1/4}$	$S^{-0.86}B^{0.24}$	0.97
u_θ^*	$S^{-3/4}B^{1/4}$	$S^{-0.82}B^{0.21}$	0.99
T_1^*	$S^{-1/2}B^{-1/2}$	$S^{-0.46}B^{-0.46}$	1.00
δ^*	$S^{-1/4}B^{-1/4}$	$S^{-0.21}B^{-0.22}$	0.95

TABLE 1. Scaling analysis and least squares inversion results for all $S > 1$ models.

The additional viscous term scales as $Eu^* l_v^{-3}$, where l_v is a relevant length scale yet to be determined.

The assertion that $l_v = \delta$ leads to $l_v = \delta \sim E^{1/2}$ independent of S, which as figure 7 demonstrates is not the case as δ has clear empirical S-dependence (see also figure 20 in appendix B, which shows the ratio of the viscous term to the incorrect scaling $Eu_h^* \delta^{*-3}$ as a function of S for all models). Alternatively, assuming that l_v represents a thin boundary layer (consistent with figure 15), then the three-term balance determines l_v to be

$$l_v \sim (E\delta^*)^{1/3}. \tag{4.18}$$

Figure 10 shows that the shear layer thickness (given in (4.8)) and the Ekman layer depth are comparable for most of our models, which are therefore in fact described

https://doi.org/10.1017/jfm.2018.999 Published online by Cambridge University Press

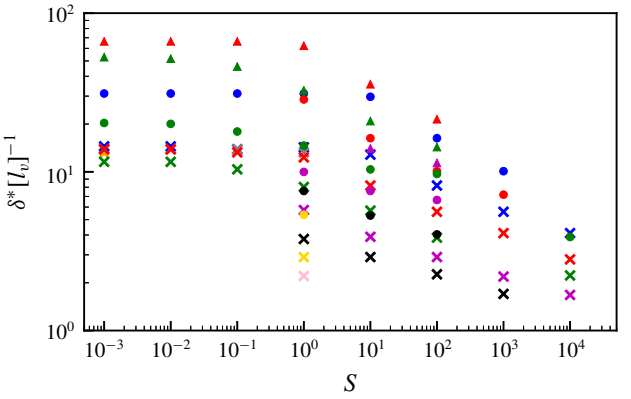


FIGURE 10. (Colour online) The shear layer thickness, δ^*, scaled by the dimensionless Ekman layer thickness estimated using (4.18) as a function of the stratification parameter, S, for all steady models. Symbol shapes represent the Ekman number, E, and colours represent the buoyancy parameter, B. The key is given in figure 6(*a*).

by a three-term (rather than a two-term) balance within the shear layer. The inclusion of viscosity within the balance in no way invalidates our analysis of the two-term scaling, but merely provides information about the characteristic length scale l_ν at which viscosity becomes important. Indeed, our derived scalings of the previous sections, confirmed empirically, appear to hold independently of the relative size of l_ν and δ^*. It is worth pointing out the physically relevant planetary regime is one in which $E \ll 1$ and $l_\nu \ll \delta$ (see also § 5), and therefore in this limit the two-term balance is appropriate for the shear layer. We speculate that there may be a different behavioural regime in which $l_\nu \gg \delta^*$ for certain choices of parameters, when viscosity balances just one other term.

4.2. *Low stratification regime*

At low S, the basic state is one of neutral stability (rather than stratification) and the flow occupies the whole shell rather than being concentrated within a thin layer. Furthermore, from (2.12) it follows also that $T_0^* \approx 0$ so that $T^* \approx T_1^*$. The dynamics of the low-S regime has previously been investigated in Zhang & Gubbins (1992), Gibbons & Gubbins (2000) and Gibbons *et al.* (2007), but these studies did not develop scaling laws as we do here using a much broader range of models in (E, S, B) space.

Within the low-S regime, we consider the energy balance of (2.14) in a steady state, by taking the inner product with $\boldsymbol{u}^*$ and integrating over the volume V. Neither the Coriolis force (which is orthogonal to the flow) nor the pressure contributes to the energy equation, as the fluid is incompressible and

$$\int_V \boldsymbol{u}^* \cdot \boldsymbol{\nabla} \hat{P} \, \mathrm{d}V = \int_V \boldsymbol{\nabla} \cdot (\hat{P} \boldsymbol{u}^*) \, \mathrm{d}V = 0 \tag{4.19}$$

because $u_r^* = 0$ on the boundary. The balance

$$B \int_V T^* u_r^* r^* \, \mathrm{d}V = E \int_V (\boldsymbol{\nabla} \times \boldsymbol{u}^*)^2 \, \mathrm{d}V \tag{4.20}$$

is then exact.

https://doi.org/10.1017/jfm.2018.999 Published online by Cambridge University Press

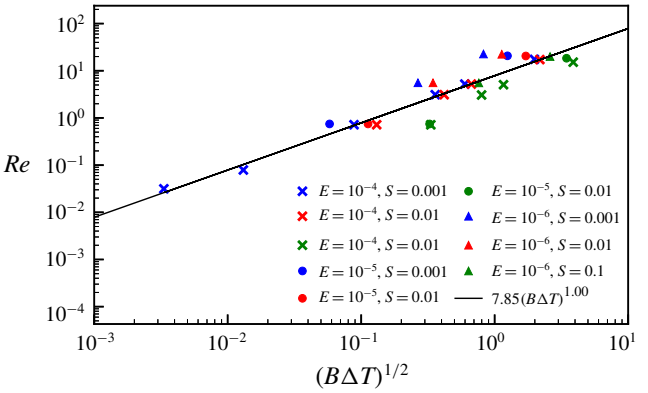


FIGURE 11. (Colour online) The Reynolds number Re against $(B\Delta T)^{1/2}$ for all low-S models. The black line shows the best empirical fit to the simulations.

Following Shishkina, Grossmann & Lohse (2016), the temperature equation (2.13) in steady state and the limit $S \to 0$ may be written

$$\boldsymbol{\nabla} \cdot (\boldsymbol{u}^* T^* - \boldsymbol{\nabla} T^*) = 0. \tag{4.21}$$

Integrating over the volume bounded by radii r^* and r_o, with $r^* < r_o$, and using the divergence theorem leads to

$$\left\langle u_r^* T^* - \frac{\partial T^*}{\partial r^*} \right\rangle = 0 \tag{4.22}$$

at any radius r^*, where $\langle \cdot \rangle$ denotes integration over all solid angles, and where we have used the fact that both u_r^* and $\langle \partial T^*/\partial r^* \rangle = \langle Y_2^2 \rangle = 0$ at $r^* = r_o$. It follows that

$$\int_V T^* u_r^* r^* \,\mathrm{d}V = \int_{r_i}^{r_o} r^{*3} \langle u_r^* T^* \rangle \,\mathrm{d}r^* = \left\langle \int_{r_i}^{r_o} r^{*3} \frac{\partial T^*}{\partial r^*} \,\mathrm{d}r^* \right\rangle, \tag{4.23}$$

and integrating by parts leads to

$$[\langle T^* \rangle (r^{*3} - 3r^{*2} + 6r^* - 6)]_{r_i}^{r_o} = A(r_o) \Delta T \tag{4.24}$$

because $T^* = 0$ on $r^* = r_i$, where $A = r_o^3 - 3r_o^2 + 6r_o - 6$ is a constant and $\Delta T = \langle T^* \rangle|_{r_o}$. The exact relation

$$BA\Delta T = E \int_V (\boldsymbol{\nabla} \times \boldsymbol{u}^*)^2 \,\mathrm{d}V \tag{4.25}$$

then follows. The viscous dissipation term on the right-hand side may be estimated as $(u^*)^2$ by assuming a viscous boundary layer length scale of $E^{1/2}$. The resulting scaling

$$u^* \sim \sqrt{B\Delta T} \tag{4.26}$$

is verified using an empirical fit to the low-S models, which gives $Re \sim (B\Delta T)^{0.50}$ ($R^2 = 0.88$) and is shown in figure 11.

We now need to estimate ΔT, which is not prescribed in models with a fixed heat-flux boundary condition, in contrast to those with a fixed temperature boundary

https://doi.org/10.1017/jfm.2018.999 Published online by Cambridge University Press

condition. We consider the thermal dissipation equation, obtained by multiplying equation (2.13) with T^* and integrating over V:

$$\int_V T^* \nabla^2 T^* \, \mathrm{d}V = \frac{1}{2} \int_V (\boldsymbol{u}^* \cdot \boldsymbol{\nabla}) T^{*2} \, \mathrm{d}V = 0 \tag{4.27}$$

since u_r^* is zero on the boundaries, and so

$$\left\langle T^* \frac{\partial T^*}{\partial r^*} \right\rangle \Bigg|_{r^*=r_o} = \int_V \boldsymbol{\nabla} \cdot (T^* \boldsymbol{\nabla} T^*) \, \mathrm{d}V = - \int_V (\boldsymbol{\nabla} T^*)^2 \, \mathrm{d}V \tag{4.28}$$

because $T^* = 0$ on the lower radial boundary. Since $\partial T^*/\partial r^*$ is prescribed as Y_2^2 on r_o, this suggests the leftmost term is comparable to ΔT. In the rightmost term, we estimate $\boldsymbol{\nabla} T^* \sim \Delta T$, which is reasonable if the majority of the dissipation occurs on the lateral length scale of $O(1)$. Assuming that most of the dissipation occurs over a radial length scale L_T at the top of the shell, the whole term is estimated to be $(\Delta T)^2 L_T$. Thus the balance in (4.28) is $\Delta T \sim (\Delta T)^2 L_T$ or

$$L_T \sim \Delta T^{-1}. \tag{4.29}$$

Furthermore, balancing advection (which is dominated by horizontal gradients with length scales of $O(1)$) and diffusion in the temperature equation (2.13) over the length scale L_T leads to $u^* \sim L_T^{-2}$. Hence $\Delta T \sim (u^*)^{1/2}$ and it therefore follows that

$$u^* \sim B^{2/3} \tag{4.30}$$

and

$$\Delta T \sim B^{1/3}. \tag{4.31}$$

The scaling for u^* is confirmed with an empirical fit to the low-S simulations, which gives $Re \sim B^{0.72}$ ($R^2 = 0.98$) and is shown in figure 12. It is worth noting that the exponent (of 2/3) in the scaling for u^* is higher than any of those reported in table 1 of Shishkina *et al.* (2016) for the related study of plane layer horizontal convection with lateral temperature variations on the lower boundary.

4.3. *Effects of the shell aspect ratio*

We have used an aspect ratio $\eta = 0.35$ in all previous models, however as we would like to apply the derived scaling laws to other shells with different aspect ratios, we now consider whether varying the geometry influences the results. To this end, we have run simulations with $\eta = 0.01$ using the parameters listed in table 6 and obtained steady-state solutions. It is apparent that the overall dynamics of the low aspect ratio models is very similar to the previously presented models, see figure 21 in appendix C. We again have two stratification regimes, a low S regime in which the dynamics occupies the entire shell and buoyancy is the dominant effect, and a high S regime in which stratification dominates and the dynamics is concentrated towards the outer boundary. In both regimes, the phase of the velocity and temperature lobes with respect to the boundary anomaly pattern is the same as in the previously discussed models. We have computed the best empirical fits to the high S models in this geometry (shown in figure 13) and confirm that these models obey the same scaling laws as derived in 4.1.3. Note that the values of the quantities shown in figures 21 and 13, are different from those shown in previous sections for the same apparent

https://doi.org/10.1017/jfm.2018.999 Published online by Cambridge University Press

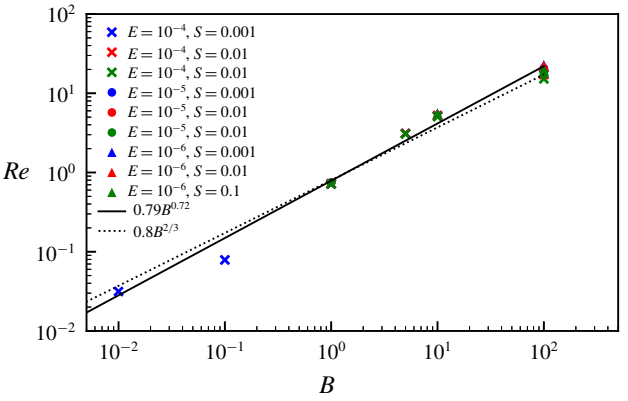


FIGURE 12. (Colour online) The Reynolds number Re against the buoyancy parameter B for all low-S models. The solid black line shows the best empirical fit to the simulations and the dotted line shows the theoretically predicted exponent from (4.30).

parameter values because the length scales in the parameters S and B differ because $d = r_o - r_i = r_o(1 - \eta)$, and averaging takes place over different volumes, meaning that for example, $B = 1$ and $St = 1000$ models at $\eta = 0.35$ and $\eta = 0.01$ are not directly comparable without accounting for geometric factors. It is worth remarking that the theoretical scaling for the horizontal velocity components (which scale as $\sim S^{-3/4}$) actually agrees slightly better with the numerics in the quasi-full sphere than the spherical shell calculations, indicating a possible weak dependence on r_i for such quantities.

5. Application of scaling laws to planetary cores

In order to apply our power law scalings to a planet, we must estimate S and B for its outer core. We write β and $\mathcal{H}$ in terms of temperature gradients at the CMB

$$\beta\, d = \left.\frac{\mathrm{d}T_{ad}}{\mathrm{d}r}\right|_{r_o} - \left.\frac{\mathrm{d}T_c}{\mathrm{d}r}\right|_{r_o}, \tag{5.1}$$

where T_{ad} is the adiabatic temperature and T_c is the core temperature at the CMB, and

$$\mathcal{H} = \left.\frac{\mathrm{d}T'}{\mathrm{d}r}\right|_{r_o} = \frac{q'}{k_c}, \tag{5.2}$$

where T' and q' are, respectively, the anomalous temperature and heat flow per unit area on the core side of the CMB. In (5.2), we have used the continuity of heat flux across the CMB along with its estimated value, q', on the mantle side; k_c is the thermal conductivity of the core. The gradients in (5.1) are evaluated using

$$\left.\frac{\mathrm{d}T_{ad}}{\mathrm{d}r}\right|_{r_o} = -\frac{\alpha_T g_c T_c}{C_p} \tag{5.3}$$

and

$$\left.\frac{\mathrm{d}T_c}{\mathrm{d}r}\right|_{r_o} = -\frac{Q_{cmb}}{A_{cmb} k_c}, \tag{5.4}$$

https://doi.org/10.1017/jfm.2018.999 Published online by Cambridge University Press

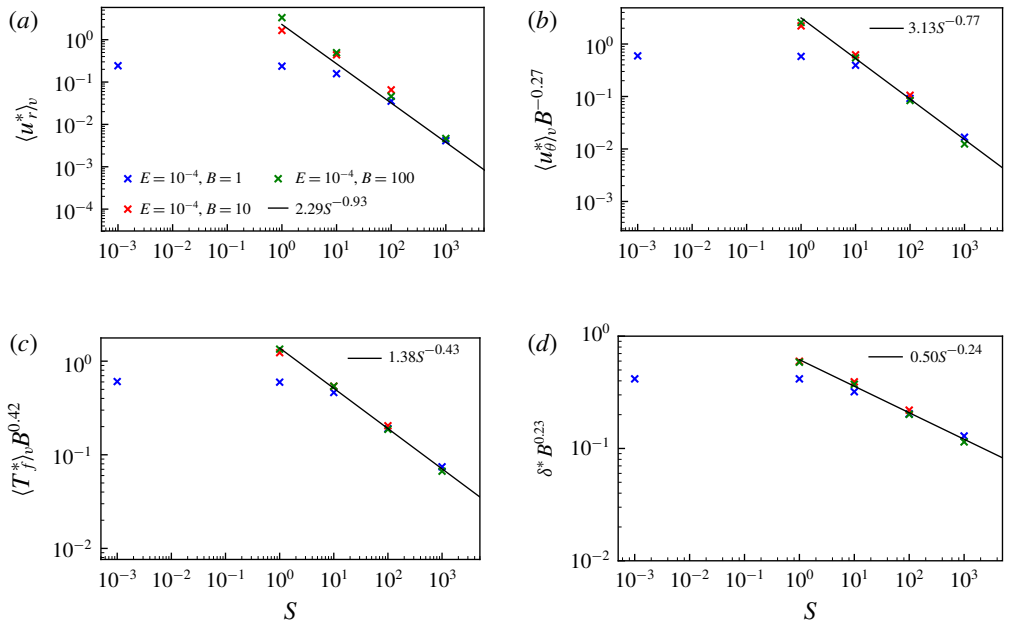


FIGURE 13. (Colour online) (*a*) Volume-averaged radial velocities, (*b*) volume-averaged azimuthal velocities, (*c*) volume-averaged temperature perturbations and (*d*) penetration depth estimates, normalised by the best empirical fit to the buoyancy parameter for all models with $\eta = 0.01$ and $S > 1$, as a function of S. The R^2 values for the fits are, respectively, 0.95, 0.99, 1.00 and 0.99. Symbol shapes represent the Ekman number, E, and colours represent the buoyancy parameter, B. The black line shows the best fitting power law in S for models at $S > 1$.

where g_c is the acceleration due to gravity at the CMB, C_p is the core specific heat, Q_{cmb} is the total CMB heat flux, A_{cmb} is the area of the CMB ($= 4\pi r_o^2$) and k_c is the core thermal conductivity. For the Earth's core, we have taken a range of plausible values from the literature, given in table 2, and calculated a range of possible S and B parameters. Estimating the stratification parameter ($S = \beta d/\mathcal{H}$) is particularly challenging due to large uncertainties on $\mathcal{H}$, the magnitude of lateral variations in CMB heat flux, whose estimate derives from relating observed shear-wave anomalies with either thermal or chemical heterogeneities. If the anomalies are attributed predominantly to thermal differences in the mantle, then the value of q' from table 2 leads to S values of $O(10^{-6})$–$O(10^{-4})$ and B values of $O(10^{17})$, placing the core in a regime in which the stratified layer is likely penetrated by unsteady boundary-driven flow.

On the other hand, if the mantle heterogeneities are attributed instead to chemical anomalies (e.g. Garnero, McNamara & Shim 2016; Lau *et al.* 2017), then $\mathcal{H}$ could be much smaller than the above estimate, rendering S plausibly $O(1)$ or above, placing the core in the stratification-dominated regime. Taking $S = 1$ for illustration with our estimates of B, applying the high S scalings (4.13)–(4.15) gives dimensional temperature perturbations of $O(10^{-3}$ K), radial velocities of $O(10^{-12}$ m s$^{-1})$, horizontal velocities of $O(10^{-7}$ m s$^{-1})$ and penetration depths of approximately 70 m, much thicker than the estimated viscosity boundary layer in Earth's core of approximately 1 m (e.g. Livermore, Bailey & Hollerbach 2016)

https://doi.org/10.1017/jfm.2018.999 Published online by Cambridge University Press

https://doi.org/10.1017/jfm.2018.999 Published online by Cambridge University Press

Parameter	Symbol	Value	Reference
Inner core radius	r_i	1221 km	Dziewonski & Anderson (1981)
Outer core radius	r_o	3480 km	Dziewonski & Anderson (1981)
Shell thickness	$d\ (=r_o-r_i)$	2259 km	Dziewonski & Anderson (1981)
Gravitational acceleration constant at CMB	g_c	10.68 ms^{-2}	Olson (2009)
Angular velocity of rotation	Ω	7.272×10^{-5} s^{-1}	Olson (2009)
Coefficient of thermal expansion	α_T	1.5×10^{-5} K^{-1}	Gubbins *et al.* (2003)
Core thermal diffusivity	κ	1.25×10^{-5} m^2 s^{-1}	Pozzo *et al.* (2012)
Core thermal conductivity	k_c	100 W m^{-1} K^{-1}	Pozzo *et al.* (2013)
Lower mantle thermal conductivity	k_m	10 W m^{-1} K^{-1}	Ammann *et al.* (2014)
Core specific heat capacity	C_p	728 J kg^{-1} K^{-1}	Gubbins *et al.* (2003)
CMB temperature	T_c	4000 K	Olson (2009)
Total CMB heat flow	Q_{cmb}	5 TW–17 TW	Lay, Hernlund & Buffett (2008), Nimmo (2015)
Total adiabatic heat flow	Q_{ad}	14 TW–16 TW	Pozzo *et al.* (2012)
Peak-to-peak anomalous CMB heat flow	q'	100 mWm^{-2}–300 mWm^{-2}	Nakagawa & Tackley (2013)

TABLE 2. Outer core and lower mantle physical, thermodynamic and transport properties used to estimate S and B for the Earth.

associated with $E = 10^{-15}$. A similar analysis for Ganymede's core, using values from table 1 of Rückriemen *et al.* (2015) and estimating $\alpha_T = 5.8 \times 10^{-5}$ based on Williams & Nimmo (2004), gives B values of $O(10^{13})$ and S values of $O(10^{-1})$–$O(1)$, assuming the mantle heterogeneities are attributed to thermal anomalies. As for the Earth, if the anomalies are predominantly due to chemical sources, these S values are significantly underestimated and Ganymede's core will be in the stratified regime.

For comparison with other works on stratified fluids, it is of interest to calculate the Brunt–Väisälä frequency, N, defined by

$$N^2 = -\frac{g}{\rho_0}\frac{\partial \rho'}{\partial r} \tag{5.5}$$

both for our models and for the planetary interiors considered. Non-dimensionalising with the same scalings as used previously gives the ratio of the Brunt–Väisälä frequency to the rotation rate

$$\frac{N}{2\Omega} = \sqrt{\frac{BE}{Pr}\frac{\partial T^*}{\partial r^*}} = \sqrt{\frac{BES}{Pr}}, \tag{5.6}$$

assuming $\partial T^*/\partial r^* \approx \partial T_0^*/\partial r^*$ due to the small magnitudes of the temperature perturbations.

Values of this ratio for our simulations vary between $O(10^{-6})$ and $O(10)$, given in tables 3–6 in appendix A. Based on our $B - S$ estimates for Earth and Ganymede, along with E and Pr estimates from table 1 of Schaeffer *et al.* (2017) for Earth ($E = 10^{-15}$, $Pr = 0.1 - 10$) and table 4 of Schubert & Soderlund (2011) for Ganymede ($E = 10^{-13}$, $Pr = 0.1$), we estimate their Brunt–Väisälä ratios of $O(1)$ for some parameter combinations, consistent with other estimates using different methods (e.g. Buffett 2014). Ignoring the dependence on E, it is worth remarking that the relationship between N and the product SB may explain why this quantity is so important in our derived theoretical scalings, with $\delta^* \sim N^{-1/4}$ and $T_1^* \sim N^{-1/2}$.

6. Discussion and conclusions

We have investigated a thermally stratified fluid in a rotating spherical shell subject to a laterally varying heat-flux pattern on the outer boundary. Converged, steady-state numerical simulations were obtained for $Pr = 1$, $E = 10^{-6}$ to $E = 10^{-3}$, $S = 10^{-3}$ to $S = 10^4$ and $B = 10^{-2}$ to $B = 10^6$. For some parameters, we obtained time-dependent solutions, which were not analysed in this study, however we were able to map the stability domain in parameter space in greater detail than any previous study. The steady-state solutions separate into two distinct dynamical regimes corresponding to low stratification parameter (S), in which buoyancy effects dominate the dynamics, and high S, in which stratification effects dominate.

In the low S regime, the inhomogeneous thermal boundary condition drives flows that are locked to the boundary pattern and penetrate most of the shell thickness. We have developed scaling relationships for the characteristic velocity Re and the temperature drop ΔT as a function of the buoyancy parameter B. In the high S regime, stratification strongly suppresses radial flow but horizontal flow is less affected. All flow is concentrated toward the outer boundary, resulting in shear layers whose thickness decreases with increasing B and S. This layer thickness represents the depth to which the boundary-driven flows penetrate the stratified fluid. We have developed scaling relations for the velocity components, temperature

https://doi.org/10.1017/jfm.2018.999 Published online by Cambridge University Press

perturbations and penetration depth as functions of the control parameters E, B and S; these are summarised in table 1. We have used these scaling relationships to extrapolate to Earth's core using a range of plausible parameters. If the Earth's mantle heterogeneities are attributed to thermal anomalies, the outer core is in the buoyancy-dominated regime and no steady-state solutions exist. In that case, it is likely that unsteady boundary-driven flows can penetrate the stratified layer. On the other hand, if such heterogeneities are linked to chemical anomalies (e.g. Garnero *et al.* 2016; Lau *et al.* 2017), the much reduced heat-flux boundary condition would likely place Earth's core in the stratification-dominated regime where penetration from steady boundary-driven flows is not possible. In that case, the shear layer thickness (i.e. the depth of penetration of boundary-driven flows through the core) is very small (of the order of a few tens of metres) compared to the stable layer thickness and the predicted velocities are several orders of magnitude smaller than those inferred from inversions of geomagnetic secular variation (e.g. Holme 2015). Since there is no reason why these inferred flows have to be generated (even in part) by mantle heterogeneities, the high S scalings suggest that we infer general convective flow magnitudes rather than boundary-driven flow magnitudes from geomagnetic data. Furthermore, it seems unlikely that chemical anomalies in the lowermost mantle are able to directly affect the magnetic field that is generated inside the core (by creating persistent non-zonal features for example) through steady boundary-driven flows.

However, the relative contributions of thermal and chemical anomalies to the boundary forcing is poorly constrained for Earth and not at all for other bodies (including Ganymede), hence the difficulty in estimating $\mathcal{H}$ and the resulting uncertainty as to which stratification regime their outer cores belong. Interestingly, this means that independent evidence of penetrating flow within the stable layer, for example through the magnetic signature of upwellings and patches of reversed magnetic flux (Gubbins 2007; Metman, Livermore & Mound 2018), may be able to discriminate between these two regimes and therefore offer evidence that constrains the heat flux on the boundary, and therefore mantle composition.

Finally, we have considered steady-state solutions in entirely stratified spherical shells with no convection or magnetic field generation; further work is needed to investigate the effects of adding these dynamics to our simplified models. The fluid dynamics problem studied here should be relevant in the uppermost region of the outer core, where no convection is expected due to stratification. Yet, it is possible that at sufficiently high B, models at $S = 1$ (the lowest stratification parameter required for our high S scalings to be applicable, and a plausible value for Earth's outer core) will be unsteady rather than steady. This transition may well occur at a B lower than our estimates for Earth's core, however, computational limitations have prevented us from reaching this transition and our simulations remain many orders of magnitude from Earth estimates. Since our systematic parameter study has revealed the different dynamical regimes that exist in the absence of internal convection, future studies will be able to benchmark against the present results and also target particular regions of parameter space to make most effective use of available computational resources.

Acknowledgements

We thank three anonymous referees for comments and suggestions that helped to improve the manuscript. This study was initiated by J.S. as his final year undergraduate project. G.A.C. was supported by NERC grant NE/M012190/1, and has received funding from Science Foundation Ireland grant 16/ERCD/4303 (iTHERC)

https://doi.org/10.1017/jfm.2018.999 Published online by Cambridge University Press

and "3D Earth - A Dynamic Living Planet" funded by ESA as a Support to Science Element (STSE). C.J.D. is supported by a NERC Independent Research Fellowship (NE/L011328/1) and P.W.L. was partially supported by NERC grant NE/G014043/1. This work was undertaken on ARC2, part of the High Performance Computing facilities at the University of Leeds, UK. Contour plots were produced in VisIt (Childs *et al.* 2012), using scripts written by J. Mound. Other figures were produced using Python's Matplotlib (Hunter 2007).

Appendix A. Summary tables

Summary tables of the model resolution, control parameters and selected output parameters for all simulations. In all cases $Pr = 1$ and the shell aspect ratio $\eta = 0.35$ for models in tables 3–5 and $\eta = 0.01$ for models in table 6. Definitions for B, S and $Ra_{\mathcal{H}}$ are given in § 2.1. The quantity $N/2\Omega$, defined in (5.6), is the ratio of the Brunt–Väisälä frequency, N, to the rotation rate Ω. The variable n_r is the number of radial points within the fluid shell, l_{max} is the maximum degree of the spherical harmonic expansion ($= m_{max}$, the maximum order of the expansion). Since $Re = Pe = \langle u^* \rangle_v$, the Rossby number is

$$Ro = 2ReE = 2\langle u^* \rangle_v E. \tag{A 1}$$

B	S	$Ra_{\mathcal{H}}$	n_r	l_{max}	$\frac{N}{2\Omega}$	Re	Ro	State
0.01	0.001	10^2	32	32	3.16×10^{-5}	0.03	6.30×10^{-6}	Steady
0.1	0.001	10^3	32	32	1.00×10^{-4}	0.08	1.58×10^{-5}	Steady
1	0.001	10^4	48	48	3.16×10^{-4}	0.72	1.44×10^{-4}	Steady
1	0.01	10^4	60	48	1.00×10^{-3}	0.72	1.44×10^{-4}	Steady
1	0.1	10^4	60	48	3.16×10^{-3}	0.72	1.43×10^{-4}	Steady
1	1	10^4	60	48	1.00×10^{-2}	0.69	1.38×10^{-4}	Steady
1	10	10^4	60	48	3.16×10^{-2}	0.41	8.14×10^{-5}	Steady
1	100	10^4	60	48	1.00×10^{-1}	0.08	1.68×10^{-5}	Steady
1	1000	10^4	60	48	3.16×10^{-1}	0.02	3.23×10^{-6}	Steady
1	10 000	10^4	60	48	1.00	0.003	5.69×10^{-7}	Steady
5	0.001	5×10^4	48	48	7.10×10^{-4}	3.11	6.22×10^{-4}	Steady
5	0.01	5×10^4	48	48	2.24×10^{-3}	3.11	6.22×10^{-4}	Steady
5	0.1	5×10^4	48	48	7.10×10^{-3}	3.06	6.13×10^{-4}	Steady
5	1	5×10^4	48	48	2.24×10^{-2}	2.49	4.98×10^{-4}	Steady
10	0.001	10^5	60	48	1.00×10^{-3}	5.22	1.04×10^{-3}	Steady
10	0.01	10^5	48	48	3.16×10^{-3}	5.22	1.04×10^{-3}	Steady
10	0.1	10^5	48	48	1.00×10^{-2}	5.01	1.01×10^{-3}	Steady
10	1	10^5	60	48	3.16×10^{-2}	3.55	7.10×10^{-4}	Steady
10	10	10^5	60	48	1.00×10^{-1}	0.84	1.69×10^{-4}	Steady
10	100	10^5	60	48	3.16×10^{-1}	0.16	3.24×10^{-5}	Steady

TABLE 3. Continued on next page.

https://doi.org/10.1017/jfm.2018.999 Published online by Cambridge University Press

10	1000	10^5	60	48	1.00	0.03	5.70×10^{-6}	Steady
10	10 000	10^5	80	64	3.16	0.005	9.58×10^{-7}	Steady
100	0.001	10^6	96	96	3.16×10^{-3}	17.45	3.49×10^{-3}	Steady
100	0.01	10^6	96	96	1.00×10^{-2}	17.25	3.45×10^{-3}	Steady
100	0.1	10^6	80	64	3.16×10^{-2}	15.21	3.04×10^{-3}	Steady
100	1	10^6	80	64	1.00×10^{-1}	8.50	1.70×10^{-3}	Steady
100	10	10^6	80	64	3.16×10^{-1}	1.66	3.33×10^{-4}	Steady
100	100	10^6	80	64	1.00	0.29	5.76×10^{-5}	Steady
100	10 000	10^6	224	224	10.0	0.008	1.60×10^{-6}	Steady
1000	0.001	10^7	256	256	—	—	—	Unsteady
1000	0.01	10^7	96	96	—	—	—	Unsteady
1000	0.1	10^7	160	160	—	—	—	Periodic
1000	1	10^7	96	96	3.16×10^{-1}	27.99	5.60×10^{-3}	Steady
1000	10	10^7	96	96	1.00	2.86	5.72×10^{-4}	Steady
1000	100	10^7	64	64	3.16	0.48	9.59×10^{-5}	Steady
1000	1000	10^7	192	192	10.0	0.08	1.60×10^{-5}	Steady
1000	10 000	10^7	224	224	31.6	0.01	2.70×10^{-6}	Steady
10 000	1	10^8	64	64	1.00	39.73	7.95×10^{-3}	Steady
10 000	10	10^8	64	64	3.16	4.79	9.58×10^{-4}	Steady
10 000	100	10^8	128	128	10.0	0.80	1.60×10^{-4}	Steady
10 000	1000	10^8	64	64	31.6	0.14	2.70×10^{-5}	Steady
100 000	1	10^9	64	64	3.16	52.57	1.05×10^{-2}	Steady
1000 000	1	10^{10}	96	96	10.0	97.37	1.95×10^{-2}	Steady

TABLE 3 (cntd). Summary of all numerical simulations with $E = 10^{-4}$.

B	S	$Ra_{\mathcal{H}}$	n_r	l_{max}	$\frac{N}{2\Omega}$	Re	Ro	State
1	0.001	10^5	48	48	1.00×10^{-4}	0.75	1.49×10^{-5}	Steady
1	0.01	10^5	48	48	3.16×10^{-4}	0.75	1.49×10^{-5}	Steady
1	0.1	10^5	48	48	1.00×10^{-3}	0.75	1.49×10^{-5}	Steady
1	1	10^5	48	48	3.16×10^{-3}	0.73	1.46×10^{-5}	Steady
1	10	10^5	64	64	1.00×10^{-2}	0.45	9.02×10^{-6}	Steady
1	100	10^5	64	64	3.16×10^{-2}	0.10	2.07×10^{-6}	Steady
1	1000	10^5	64	64	0.1	0.02	4.51×10^{-7}	Steady
10	0.001	10^6	48	48	3.16×10^{-4}	5.49	1.10×10^{-4}	Steady
10	1	10^6	48	48	1.00×10^{-2}	3.96	7.92×10^{-5}	Steady
10	10	10^6	64	64	3.16×10^{-2}	1.04	2.07×10^{-5}	Steady
10	100	10^6	64	64	1.00×10^{-1}	0.23	4.51×10^{-6}	Steady
10	1000	10^6	64	64	3.16×10^{-1}	0.05	9.12×10^{-7}	Steady
100	0.001	10^7	48	48	1.00×10^{-3}	20.74	4.15×10^{-4}	Steady
100	0.01	10^7	96	96	3.16×10^{-3}	20.57	4.11×10^{-4}	Steady
100	0.1	10^7	96	96	1.00×10^{-2}	18.43	3.69×10^{-4}	Steady
100	1	10^7	48	48	3.16×10^{-2}	10.20	2.04×10^{-4}	Steady
100	10	10^7	96	96	1.00×10^{-1}	2.37	4.75×10^{-5}	Steady
100	100	10^7	96	96	3.16×10^{-1}	0.47	9.35×10^{-6}	Steady
100	10 000	10^7	192	192	3.16	0.02	3.10×10^{-7}	Steady
1000	0.01	10^8	160	160	—	—	—	Unsteady
1000	0.1	10^8	128	128	—	—	—	Unsteady

TABLE 4. Continued on next page.

https://doi.org/10.1017/jfm.2018.999 Published online by Cambridge University Press

1000	1	10^8	128	128	1.00×10^{-1}	43.64	8.73×10^{-4}	Steady
1000	10	10^8	128	128	3.16×10^{-1}	6.00	1.20×10^{-4}	Steady
1000	100	10^8	128	128	1.00	0.87	1.75×10^{-5}	Steady
10 000	0.01	10^9	128	128	—	—	—	Unsteady
10 000	0.1	10^9	128	128	—	—	—	Unsteady
10 000	1	10^9	128	128	3.16×10^{-1}	218.25	4.36×10^{-3}	Steady
10 000	10	10^9	128	128	10.0	10.36	2.07×10^{-4}	Steady
10 000	100	10^9	128	128	3.16	1.55	3.10×10^{-5}	Steady
100 000	1	10^{10}	64	64	1.00	420.48	8.41×10^{-3}	Steady

TABLE 4 (cntd). Summary of all numerical simulations with $E = 10^{-5}$.

B	S	$Ra_{\mathcal{H}}$	n_r	l_{max}	$\frac{N}{2\Omega}$	Re	Ro	State
10	0.001	10^7	96	96	1.00×10^{-4}	5.57	1.11×10^{-5}	Steady
10	0.01	10^7	96	96	3.16×10^{-4}	5.56	1.11×10^{-5}	Steady
10	0.1	10^7	96	96	1.00×10^{-3}	5.54	1.11×10^{-5}	Steady
10	1	10^7	96	96	3.16×10^{-3}	4.17	8.34×10^{-6}	Steady
10	10	10^7	96	96	1.00×10^{-2}	1.13	2.25×10^{-6}	Steady
10	100	10^7	192	192	3.16×10^{-2}	0.27	5.33×10^{-7}	Steady
100	0.001	10^8	128	128	3.16×10^{-4}	22.69	4.54×10^{-5}	Steady
100	0.01	10^8	128	128	1.00×10^{-3}	22.37	4.47×10^{-5}	Steady
100	0.1	10^8	128	128	3.16×10^{-3}	20.04	4.01×10^{-5}	Steady
100	1	10^8	96	96	1.00×10^{-2}	11.43	2.29×10^{-5}	Steady
100	10	10^8	96	96	3.16×10^{-2}	2.81	5.26×10^{-7}	Steady
1000	0.1	10^9	160	160	—	—	—	Unsteady
1000	10	10^9	96	96	1.00×10^{-1}	9.91	1.98×10^{-5}	Steady
1000	100	10^9	224	224	3.16×10^{-1}	1.34	2.68×10^{-6}	Steady

TABLE 5. Summary of all numerical simulations with $E = 10^{-6}$.

E	B	S	$Ra_{\mathcal{H}}$	n_r	l_{max}	$\frac{N}{2\Omega}$	Re	Ro
10^{-4}	1	0.001	10 000	48	48	3.16×10^{-4}	0.300872	0.601744×10^{-4}
10^{-4}	1	1	10 000	48	48	1.00×10^{-2}	0.295070	0.590139×10^{-4}
10^{-4}	1	10	10 000	48	48	3.16×10^{-2}	0.217627	0.435254×10^{-4}
10^{-4}	1	100	10 000	48	48	1.00×10^{-1}	0.064906	0.129813×10^{-4}
10^{-4}	1	1000	10 000	48	48	3.16×10^{-1}	0.013037	0.260743×10^{-5}
10^{-4}	10	1	10 000	48	48	3.16×10^{-2}	2.243120	0.448624×10^{-3}
10^{-4}	10	10	10 000	48	48	1.00×10^{-2}	1.056216	0.211243×10^{-3}
10^{-4}	10	100	10 000	48	48	3.16×10^{-1}	0.594569	0.118914×10^{-3}
10^{-4}	100	1	10 000	48	48	1.00×10^{-1}	11.922864	0.238457×10^{-2}
10^{-4}	100	10	10 000	48	48	3.16×10^{-1}	11.787036	0.235741×10^{-2}
10^{-4}	100	100	10 000	48	48	1.00	0.243352	0.486704×10^{-4}
10^{-4}	100	1000	10 000	48	48	3.16	0.041440	0.828798×10^{-5}

TABLE 6. Summary of all numerical simulations with $E = 10^{-4}$ and shell aspect ratio $\eta = 0.01$.

Appendix B. Scaling analysis figures

Figures 14–20 show examples of the term balances in the vorticity and temperature equations for a few representative high and low S models. These figures are used

https://doi.org/10.1017/jfm.2018.999 Published online by Cambridge University Press

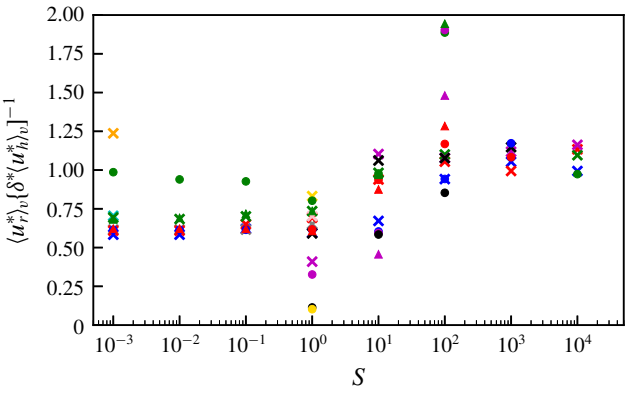


FIGURE 14. (Colour online) Radial velocity scaled by $\delta^* \langle u_h^* \rangle_v$, where $\langle u_h^* \rangle_v$ is the average volume-averaged horizontal velocity, as a function of the stratification parameter, S, for all steady models. Symbol shapes represent the Ekman number, E, and colours represent the buoyancy parameter, B. The key is given in figure 6(*a*).

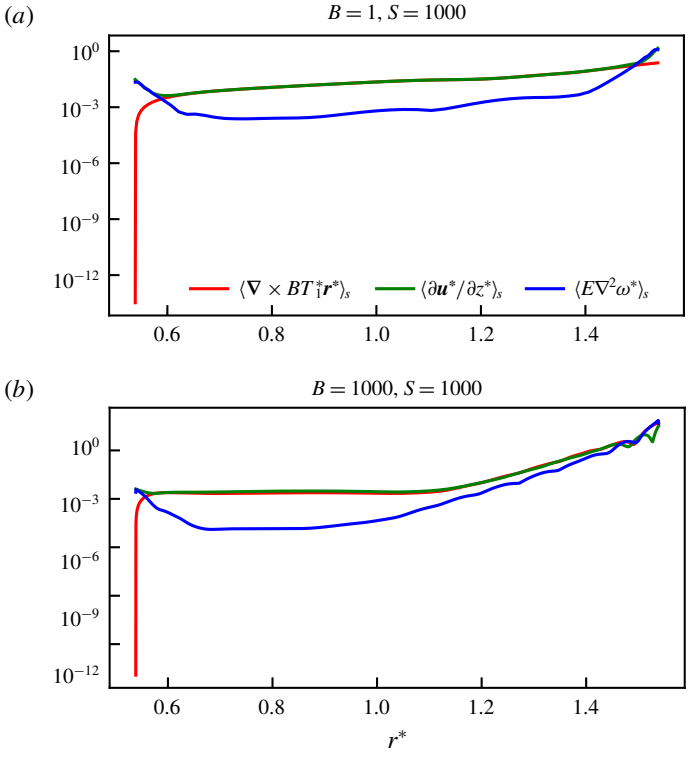


FIGURE 15. (Colour online) All terms (denoted by line colour) in the dimensionless vorticity equation as a function of radius for two representative $E = 10^{-4}$ models at high stratification parameter ($S = 1000$) and (*a*) $B = 1$ and (*b*) $B = 1000$.

https://doi.org/10.1017/jfm.2018.999 Published online by Cambridge University Press

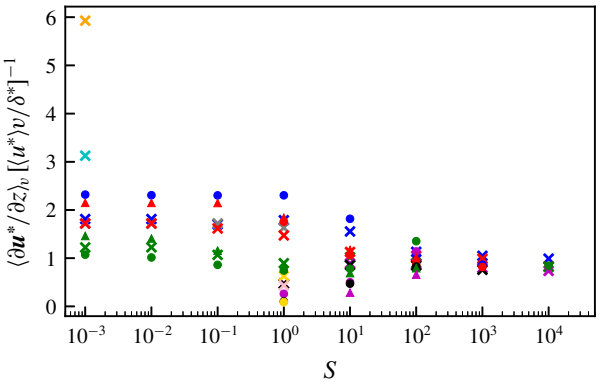


FIGURE 16. (Colour online) Volume-averaged Coriolis term of the vorticity equation ($\partial \boldsymbol{u}^*/\partial z^*$), scaled by our approximation to that term ($\langle u^* \rangle_v/\delta^*$), as a function of the stratification parameter, S, for all steady models. Symbol shapes represent the Ekman number, E, and colours represent the buoyancy parameter, B. The key is given in figure 6(*a*).

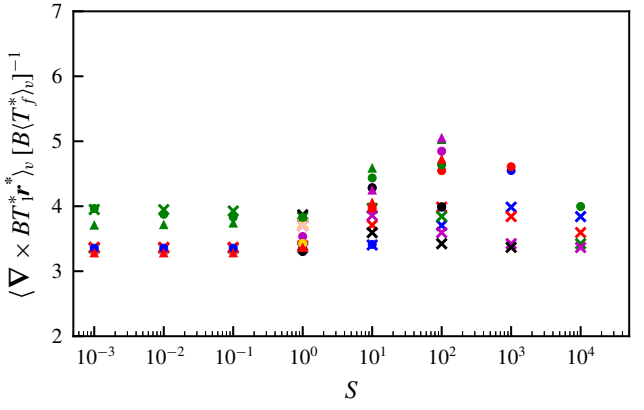


FIGURE 17. (Colour online) Volume-averaged buoyancy term of the vorticity equation ($\boldsymbol{\nabla} \times BT_1^* \boldsymbol{r}^*$), scaled by our approximation to that term ($B\langle T_f^* \rangle_v$), as a function of the stratification parameter, S, for all steady models. Symbol shapes represent the Ekman number, E, and colours represent the buoyancy parameter, B. The key is given in figure 6(*a*).

to verify our scaling predictions (i.e. that we have used the correct length scales in various terms) and to justify only considering certain terms in the governing equation in the scaling analyses, as they make clear that the balances we consider are both applicable in our two S regimes, appropriately scaled in our analysis and that our volume-averaged model diagnostics are appropriate (as we could have chosen other diagnostic outputs from the simulations).

https://doi.org/10.1017/jfm.2018.999 Published online by Cambridge University Press

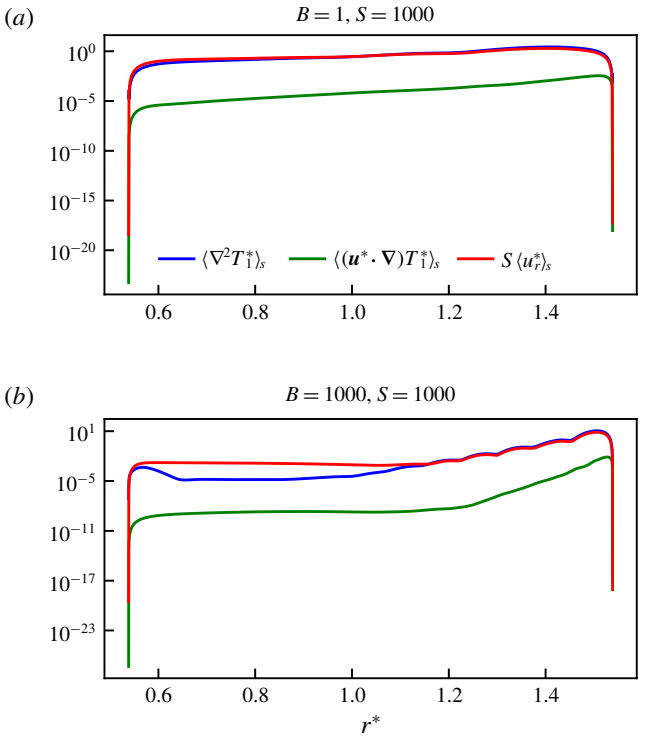


FIGURE 18. (Colour online) All terms (denoted by line colour) in the dimensionless temperature equation as a function of radius for two representative $E = 10^{-4}$ models at high stratification parameter ($S = 1000$) and (*a*) $B = 1$ and (*b*) $B = 1000$.

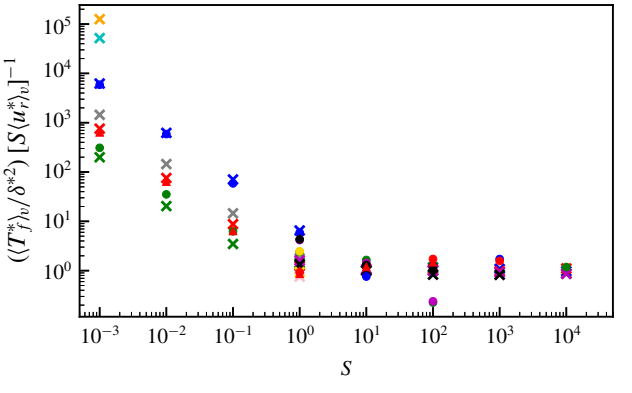


FIGURE 19. (Colour online) Ratio of the two dominant terms in the temperature equation as a function of the stratification parameter, S, for all steady models. Symbol shapes represent the Ekman number, E, and colours represent the buoyancy parameter, B. The key is given in figure 6(*a*).

https://doi.org/10.1017/jfm.2018.999 Published online by Cambridge University Press

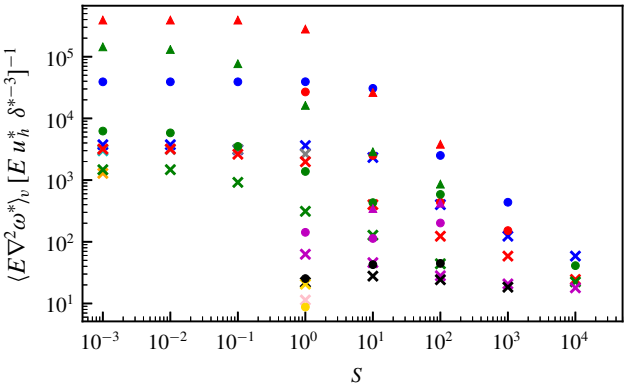


FIGURE 20. (Colour online) Volume-averaged viscous term of the vorticity equation ($E\nabla^2\omega^*$), scaled by the (incorrect) approximation to that term ($Eu_h^*\delta^{*-3}$), as a function of the stratification parameter, S, for all steady models. Symbol shapes represent the Ekman number, E, and colours represent the buoyancy parameter, B. The key is given in figure 6(*a*).

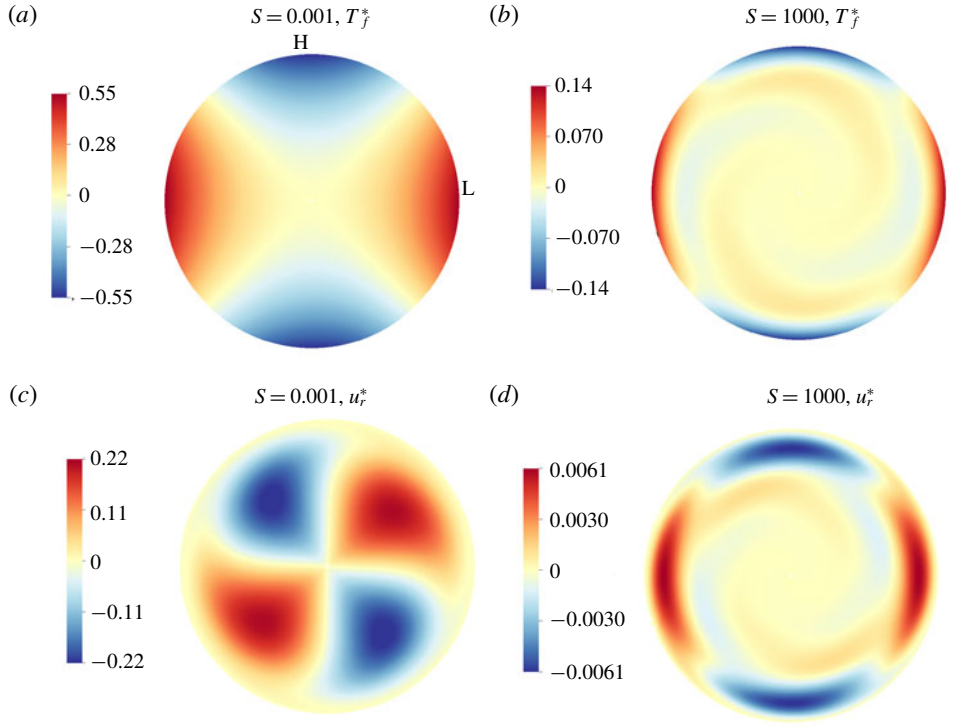


FIGURE 21. For caption see next page.

Appendix C. Low shell aspect ratio dynamics

Figure 21 shows the effects on the dynamics of low aspect ratio models.

https://doi.org/10.1017/jfm.2018.999 Published online by Cambridge University Press

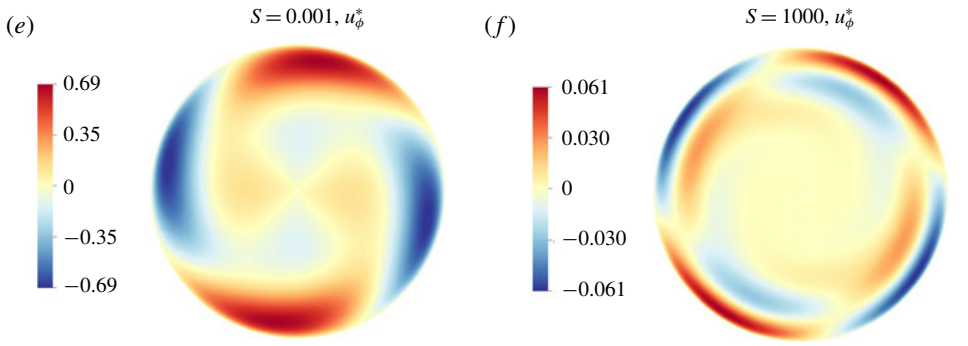


FIGURE 21 (cntd). (Colour online) Equatorial plots of T_f^* (*a*,*b*), u_r^* (*c*,*d*) and u_ϕ^* (*e*,*f*) for models with shell aspect ratio $\eta = 0.01$ at $E = 10^{-4}$, $B = 1$ and $S = 0.001$ (*a*,*c*,*e*) and 1000 (*b*,*d*,*f*). Red indicates positive values and blue indicates negative values. Note the different colour scales. Locations of high (H) and low (L) outward heat flux are shown on the top left.

REFERENCES

AMIT, H., CHOBLET, G., OLSON, P., MONTEUX, J., DESCHAMPS, F., LANGLAIS, B. & TOBIE, G. 2015 Towards more realistic core-mantle boundary heat flux patterns: a source of diversity in planetary dynamos. *Prog. Earth Planetary Sci.* **2** (1), 26.

AMMANN, M. W., WALKER, A. M., STACKHOUSE, S., WOOKEY, J., FORTE, A. M., BRODHOLT, J. P. & DOBSON, D. P. 2014 Variation of thermal conductivity and heat flux at the Earth's core mantle boundary. *Earth Planet. Sci. Lett.* **390**, 175–185.

AURNOU, J. M. & AUBERT, J. 2011 End-member models of boundary-modulated convective dynamos. *Phys. Earth Planet. Inter.* **187** (3), 353–363.

BUFFETT, B. 2014 Geomagnetic fluctuations reveal stable stratification at the top of the Earth's core. *Nature* **507** (7493), 484–487.

BUFFETT, B. A. & SEAGLE, C. T. 2010 Stratification of the top of the core due to chemical interactions with the mantle. *J. Geophys. Res.* **115**, B04407.

CHANDRASEKHAR, S. 1961 *Hydrodynamic and Hydromagnetic Stability*. OUP.

CHILDS, H., BRUGGER, E., WHITLOCK, B., MEREDITH, J., AHERN, S., BONNELL, K., MILLER, M., WEBER, G. H., HARRISON, C., PUGMIRE, D., FOGAL, T., GARTH, C., SANDERSON, A., BETHEL, E. W., DURANT, M., CAMP, D., FAVREK, J. M., RUBEL, O., NAVRÁTIL, P., WHEELER, M., SELBY, P. & VIVODTZEV, F. 2012 Visit: an end-user tool for visualizing and analyzing very large data. *Tech. Rep.*, Ernest Orlando Lawrence Berkeley, National Laboratory, Berkeley, CA (US).

CHRISTENSEN, U. R. 2006 A deep dynamo generating Mercury/'s magnetic field. *Nature* **444** (7122), 1056–1058.

CHRISTENSEN, U. R. & WICHT, J. 2008 Models of magnetic field generation in partly stable planetary cores: applications to Mercury and Saturn. *Icarus* **196** (1), 16–34.

DAVIES, C. J., GUBBINS, D. & JIMACK, P. K. 2009 Convection in a rapidly rotating spherical shell with an imposed laterally varying thermal boundary condition. *J. Fluid Mech.* **641**, 335–358.

DAVIES, C., POZZO, M., GUBBINS, D. & ALFÈ, D. 2015 Constraints from material properties on the dynamics and evolution of Earth's core. *Nature Geosci.* **8** (9), 678.

DAVIES, C. J., GUBBINS, D. & JIMACK, P. K. 2011 Scalability of pseudospectral methods for geodynamo simulations. *Concurrency Comput.* **23** (1), 38–56.

DZIEWONSKI, A. M. & ANDERSON, D. L. 1981 Preliminary reference Earth model. *Phys. Earth Planet. Inter.* **25**, 297–356.

DZIEWONSKI, A. M., LEKIC, V. & ROMANOWICZ, B. A. 2010 Mantle anchor structure: an argument for bottom up tectonics. *Earth Planet. Sci. Lett.* **299** (1–2), 69–79.

https://doi.org/10.1017/jfm.2018.999 Published online by Cambridge University Press

GARNERO, E. J., MCNAMARA, A. K. & SHIM, S.-H. 2016 Continent-sized anomalous zones with low seismic velocity at the base of Earth's mantle. *Nature Geosci.* **9** (7), 481–489.

GIBBONS, S. J., GUBBINS, D. & ZHANG, K. 2007 Convection in rotating spherical fluid shells with inhomogeneous heat flux at the outer boundary. *Geophys. Astrophys. Fluid Dyn.* **101** (5–6), 347–370.

GIBBONS, S. J. & GUBBINS, D. 2000 Convection in the Earth's core driven by lateral variations in the core-mantle boundary heat flux. *Geophys. J. Intl* **142**, 631–642.

GUBBINS, D. 2007 Geomagnetic constraints on stratification at the top of Earth's core. *EPS* **59** (7), 661–664.

GUBBINS, D., ALFÈ, D., DAVIES, C. & POZZO, M. 2015 On core convection and the geodynamo: effects of high electrical and thermal conductivity. *Phys. Earth Planet. Intl* **247**, 56–64.

GUBBINS, D., ALFÈ, D., MASTERS, G., PRICE, D. & GILLAN, M. J. 2003 Can the earth's dynamo run on heat alone? *Geophys. J. Intl* **155** (2), 609–622.

GUBBINS, D & DAVIES, C. J. 2013 The stratified layer at the core–mantle boundary caused by barodiffusion of oxygen, sulphur and silicon. *Phys. Earth Planet. Inter.* **215**, 21–28.

GUBBINS, D., WILLIS, A. P. & SREENIVASAN, B. 2007 Correlation of Earth's magnetic field with lower mantle thermal and seismic structure. *Phys. Earth Planet. Intl* **162**, 256–260.

HOLME, R. 2015 Large-scale flow in the core. In *Treatise on Geophysics* (ed. G. Schubert), vol. 8, pp. 91–113. Elsevier.

HUNTER, J. D. 2007 Matplotlib: a 2D graphics environment. *Comput. Sci. Engng* **9** (3), 90–95.

LAU, H. C. P., MITROVICA, J. X., DAVIS, J. L., TROMP, J., YANG, H.-Y. & AL-ATTAR, D. 2017 Tidal tomography constrains earth's deep-mantle buoyancy. *Nature* **551** (7680), 321.

LAY, T., HERNLUND, J. & BUFFETT, B. A. 2008 Core–mantle boundary heat flow. *Nature Geosci.* **1** (1), 25–32.

LIVERMORE, P. W., BAILEY, L. M. & HOLLERBACH, R. 2016 A comparison of no-slip, stress-free and inviscid models of rapidly rotating fluid in a spherical shell. *Sci. Rep.* **6**, 22812.

MATSUI, H., HEIEN, E., AUBERT, J., AURNOU, J. M., AVERY, M., BROWN, B., BUFFETT, B. A., BUSSE, F., CHRISTENSEN, U. R., DAVIES, C. J., FEATHERSTONE, N., GASTINE, T., GLATZMAIER, G. A., GUBBINS, D., GUERMOND, J.-L., HAYASHI, Y.-Y., HOLLERBACH, R., HWANG, L. J., JACKSON, A., JONES, C. A., JIANG, W., KELLOGG, L. H., KUANG, W., LANDEAU, M., MARTI, P., OLSON, P., RIBEIRO, A., SASAKI, Y., SCHAEFFER, N., SIMITEV, R. D., SHEYKO, A., SILVA, L., STANLEY, S., TAKAHASHI, F., TAKEHIRO, S., WICHT, J. & WILLIS, A. P. 2016 Performance benchmarks for a next generation numerical dynamo model. *Geochem. Geophys. Geosyst.* **17** (5), 1586–1607.

METMAN, M. C., LIVERMORE, P. W. & MOUND, J. E. 2018 The reversed and normal flux contributions to axial dipole decay for 1880–2015. *Phys. Earth Planet. Inter.* **276**, 106–117.

MOUND, J. E. & DAVIES, C. J. 2017 Heat transfer in rapidly rotating convection with heterogeneous thermal boundary conditions. *J. Fluid Mech.* **828**, 601–629.

NAKAGAWA, T. 2011 Effect of a stably stratified layer near the outer boundary in numerical simulations of a magnetohydrodynamic dynamo in a rotating spherical shell and its implications for Earth's core. *Phys. Earth Planet. Inter.* **187** (3), 342–352.

NAKAGAWA, T. 2015 An implication for the origin of stratification below the core–mantle boundary region in numerical dynamo simulations in a rotating spherical shell. *Phys. Earth Planet. Inter.* **247**, 94–104.

NAKAGAWA, T. & TACKLEY, P. J. 2008 Lateral variations in CMB heat flux and deep mantle seismic velocity caused by a thermal–chemical-phase boundary layer in 3D spherical convection. *Earth Planet. Sci. Lett.* **271** (1–4), 348–358.

NAKAGAWA, T. & TACKLEY, P. J. 2013 Implications of high core thermal conductivity on Earth's coupled mantle and core evolution. *Geophys. Res. Lett.* **40** (11), 2652–2656.

NIMMO, F. 2015 Thermal and compositional evolution of the core. In *Treatise on Geophysics*, 2nd edn. (ed. G. Schubert), vol. 9, pp. 209–219. Elsevier.

OLSON, P. 2009 Core dynamics. In *Treatise on Geophysics*, 1st edn. (ed. G. Schubert), vol. 8. Elsevier.

OLSON, P. & CHRISTENSEN, U. R. 2002 The time-averaged magnetic field in numerical dynamos with non-uniform boundary heat flow. *Geophys. J. Intl* **151** (3), 809–823.

https://doi.org/10.1017/jfm.2018.999 Published online by Cambridge University Press

OLSON, P., DEGUEN, R., RUDOLPH, M. L. & ZHONG, S. 2015 Core evolution driven by mantle global circulation. *Phys. Earth Planet. Intl* **243**, 44–55.

OLSON, P., LANDEAU, M. & REYNOLDS, E. 2017 Dynamo tests for stratification below the core-mantle boundary. *Phys. Earth Planet. Inter.* **271**, 1–18.

OTERO, J., WITTENBERG, R. W., WORTHING, R. A. & DOERING, C. R. 2002 Bounds on Rayleigh–Bénard convection with an imposed heat flux. *J. Fluid Mech.* **473**, 191–199.

PAPARELLA, F. & YOUNG, W. R. 2002 Horizontal convection is non-turbulent. *J. Fluid Mech.* **466**, 205–214.

POZZO, M., DAVIES, C., GUBBINS, D. & ALFÈ, D. 2012 Thermal and electrical conductivity of iron at Earth's core conditions. *Nature* **485**, 355–358.

POZZO, M., DAVIES, C., GUBBINS, D. & ALFÈ, D. 2013 Transport properties for liquid silicon-oxygen-iron mixtures at Earth's core conditions. *Phys. Rev.* B **87** (1), 014110.

RÜCKRIEMEN, T., BREUER, D. & SPOHN, T. 2015 The Fe snow regime in Ganymede's core: a deep-seated dynamo below a stable snow zone. *J. Geophys. Res.* **120** (6), 1095–1118.

SAHOO, S. & SREENIVASAN, B. 2017 On the effect of laterally varying boundary heat flux on rapidly rotating spherical shell convection. *Phys. Fluids* **29** (8), 086602.

SCHAEFFER, N., JAULT, D., NATAF, H.-C. & FOURNIER, A. 2017 Turbulent geodynamo simulations: a leap towards Earth's core. *Geophys. J. Intl* **211** (1), 1–29.

SCHUBERT, G. & SODERLUND, K. M. 2011 Planetary magnetic fields: observations and models. *Phys. Earth Planet. Inter.* **187** (3–4), 92–108.

SHEARD, G. J., HUSSAM, W. K. & TSAI, T. 2016 Linear stability and energetics of rotating radial horizontal convection. *J. Fluid Mech.* **795**, 1–35.

SHISHKINA, O. 2017 Mean flow structure in horizontal convection. *J. Fluid Mech.* **812**, 525–540.

SHISHKINA, O., GROSSMANN, S. & LOHSE, D. 2016 Heat and momentum transport scalings in horizontal convection. *Geophys. Res. Lett.* **43** (3), 1219–1225.

SIGGERS, J. H., KERSWELL, R. R. & BALMFORTH, N. J. 2004 Bounds on horizontal convection. *J. Fluid Mech.* **517**, 55–70.

SREENIVASAN, B. 2009 On dynamo action produced by boundary thermal coupling. *Phys. Earth Planet. Inter.* **177** (3), 130–138.

SREENIVASAN, B. & GUBBINS, D. 2008 Dynamos with weakly convecting outer layers: implications for core-mantle boundary interaction. *Geophys. Astrophys. Fluid Dyn.* **102** (4), 395–407.

SREENIVASAN, B. & GUBBINS, D. 2011 On mantle-induced heat flow variations at the inner core boundary. *Phys. Earth Planet. Intl* **187** (3), 336–341.

STANLEY, S. & GLATZMAIER, G. A. 2010 Dynamo models for planets other than earth. *Space Sci. Rev.* **152**, 617–649.

STANLEY, S. & MOHAMMADI, A. 2008 Effects of an outer thin stably stratified layer on planetary dynamos. *Phys. Earth Planet. Inter.* **168** (3), 179–190.

STEVENSON, D. J. 2001 Mars' core and magnetism. *Nature* **412** (6843), 214–219.

TAKAHASHI, F., TSUNAKAWA, H., MATSUSHIMA, M., MOCHIZUKI, N. & HONKURA, Y. 2008 Effects of thermally heterogeneous structure in the lowermost mantle on the geomagnetic field strength. *Earth Planet. Sci. Lett.* **272** (3), 738–746.

TAKEHIRO, S.-I. & LISTER, J. R. 2001 Penetration of columnar convection into an outer stably stratified layer in rapidly rotating spherical fluid shells. *Earth Planet. Sci. Lett.* **187** (3), 357–366.

WILLIAMS, J.-P. & NIMMO, F. 2004 Thermal evolution of the Martian core: implications for an early dynamo. *Geology* **32** (2), 97–100.

WILLIS, A. P., SREENIVASAN, B. & GUBBINS, D. 2007 Thermal core-mantle interaction: exploring regimes for 'locked' dynamo action. *Phys. Earth Planet. Intl* **165** (1), 83–92.

ZHANG, K. & GUBBINS, D. 1992 On convection in the Earth's core driven by lateral temperature variations in the lower mantle. *Geophys. J. Intl* **108** (1), 247–255.

ZHANG, K. & GUBBINS, D. 1993 Convection in a rotating spherical fluid shell with an inhomogeneous temperature boundary condition at infinite Prandtl number. *J. Fluid Mech.* **250**, 209–232.

https://doi.org/10.1017/jfm.2018.999 Published online by Cambridge University Press